DESIGN TECHNIQUES FOR TERAHERTZ PLASMONIC FILTERS

by

Andrew Keith Paulsen

A thesis submitted to the faculty of
The University of Utah
in partial fulfillment of the requirements for the degree of

Master of Science

Department of Electrical and Computer Engineering

The University of Utah

December 2014

The University of Utah Graduate School

STATEMENT OF THESIS APPROVAL

The thesis of **Andrew Keith Paulsen**

has been approved by the following supervisory committee members:

Ajay Nahata	, Chair	**7/18/14** Date Approved
Steven Blair	, Member	**7/18/14** Date Approved
David Schurig	, Member	**7/18/14** Date Approved

and by **Gianluca Lazzi** , Chair/Dean of

the Department/College/School of **Electrical and Computer Engineering**

and by David B. Kieda, Dean of The Graduate School.

ABSTRACT

Wireless communication systems in the terahertz (THz) frequency range promise to dramatically increase available bandwidth in the electromagnetic spectrum. These wireless systems will require filtering techniques capable of operating in this relatively unused part of the spectrum. In pushing towards more advanced filtering techniques, we demonstrate a terahertz filter design methodology based upon k-space that shows more complex filters such as band-pass, comb-pass and polarization-dependent filters. Using this design flow, we demonstrate: setting the center frequency and bandwidth in THz band-pass filters, controlling the individual magnitudes of each resonant peak in a comb filter, adjusting the transmittance of a filter at two different frequencies by spatially rotating the filter, and varying the transmittance at a single frequency by changing the polarization angle of incoming radiation. We believe this new k-space filter design methodology will help to create more complex filters that will find application in wireless THz communication systems.

TABLE OF CONTENTS

LIST OF FIGURES

ACKNOWLEDGEMENTS

I would like to thank my Father for all he has done throughout my life to help and teach me; from our first heart monitor project in 2nd grade to the beginning years of my career as an electrical engineer. Thank you for fostering my love of this field; I wouldn't be here without your example and guidance.

I would also like to thank my advisor, Dr. Ajay Nahata, whose impressive teaching in lasers and optics has given me a solid foundation from which to work. But more importantly, you have taught me resilience, determination, and a level-headed professionalism in the face of hard problems and long odds. I hope one day to build up the work ethic, commitment, and character you have exemplified to me.

Additionally, I would like to thank the University of Utah MRSEC for financially supporting my research, without which none of this work would have been possible. Thank you.

CHAPTER 1

INTRODUCTION

1.1 The Terahertz Region

Terahertz (THz) radiation spans a portion of the electromagnetic spectrum above 50 GHz where traditional electronic and microwave devices operate and below infrared wavelengths of 30 um corresponding to a frequency of 10 THz. This largely untapped portion of the spectrum holds promise for technological innovations such as expanded capacity in wireless infrastructure and enhanced security screenings. The challenges to unlocking these innovations are not trivial; the lossy nature of the Earth's atmosphere in the THz region has shown to be a formidable challenge and many materials that work well in other frequency regimes falter in this band of frequencies. This thesis aims to broaden the devices and techniques available in the THz region, specifically in the area of THz filter design and fabrication.

Optical devices that operate in the THz regime are few in number due to the poor optical properties of most materials in this range of the EM spectrum. This problem with optical material properties has resulted in what has largely been called the THz gap which ranges from 100GHz to 10THz [1]. In the last decade, advances in THz technology have exploded with the development of new ways of thinking about materials and the way devices are made. Instead of relying on the bulk optical properties of materials,

researchers are engineering the properties of materials by designing subwavelength patterning for devices. This allows far better control over the optical properties of devices and enables enhanced performance compared to traditional materials.

The focus on enabling THz devices is driven by compelling applications in medical and security imaging, where THz waves can be used to view certain tumors [2], sense dangerous chemical compounds [3], and enhance detection of metallic objects at security check points [4]. Farther reaching applications in communications might be pushing bandwidths and data rates from the traditional GHz range by orders of magnitude as devices begin to work effectively in the THz region [5]. Some of the key building blocks in such a THz communication systems are missing or need further refinement before they are a viable solution. One such key element that needs refinement is a filter design methodology that allows system designers flexibility in designing arbitrary filter shapes [6]. The ability to design arbitrary and complicated filters is employed routinely in standard digital electronics and enables the wireless devices used in the radio and microwave portions of the EM spectrum.

1.2 THz Communication

Efficient use of the electromagnetic spectrum is becoming an increasingly difficult challenge as wireless and mobile devices proliferate in society. Edholm's law, which has been seen to mirror the trend seen in Moore's law, suggests that demands on bandwidth will double every eighteen months [7]. In the face of this daunting challenge, it is clear that innovative techniques are required not only to optimize the use of currently allocated spectral bands but to push to higher and higher frequencies in the EM spectrum. The problems associated with using higher frequencies are not trivial, as path loss in the

atmosphere increases dramatically due to strong absorption resonances in oxygen molecules; humidity and rain fade also greatly attenuate signals in the high GHz and THz [5]. Despite these challenges, research groups and companies are pushing forward with efforts to create wireless systems that operate in the millimeter wave regime, from 30 GHz to 300GHz [8].

These millimeter wave devices and systems are targeted to solve one of the cellular industries greatest hurdles, backhaul links to connect small modular "pico-cell" networks together [9]. The proposed use case for such a network topology are urban areas where the intersection of large groups of users and a high density of physical infrastructure warrant short path and high data rate links. Infrastructure such as lamp posts and telephone poles allow for line of sight path distances less than 100 meters, perfect for directional antenna systems operating in the millimeter wave range. These systems are slated to support the large data pipes that will interconnect the various pico-cell networks with desired data rates in the 10s of Gbits/s [6]. Low-loss windows in the spectrum have already been allocated by the FCC with an unlicensed band at 30GHz and a licensed band at 60GHz [10]. The progression of millimeter wave wireless backhaul networks has a promising future in delivering a viable solution to urban areas and pushing the frontier of Edholm's law for the next 3–5 years.

The question now becomes whether the technology behind millimeter wave systems be applied to even higher frequencies in the THz region of the spectrum from .1 to 10 THz. Historically, the answer appears to be no. Efficiency curves for traditional microwave electronic devices have sharp drop offs as frequencies rise into the THz range due to parasitic resistance and capacitance in device implementation [5]. The current

millimeter devices and systems operate at the very limit of microwave electronics. A radically different technology is the THz quantum cascade (QC) laser which offers a possible solution from a laser design perspective. These devices can output hundreds of milliwatts but require operating temperatures to be well below freezing [11]. The output power of most THz QC lasers also drops significantly at lower frequencies close to 1THz. The operating gap between traditional electronics and QC lasers can be filled using ultrafast and nonlinear optic techniques to span the entirety of the THz Gap from .1-10THz. Using a mode-locked femtosecond laser, THz radiation can be generated from Photoconductive Dipole Antennas (PDA) [12] and other nonlinear materials [13]. These methods of THz generation have been explored extensively in the past two decades and are used to perform coherent Time Domain THz Spectroscopy (THz TDS). THz wireless communication represents a pathway forward in the next 5-10 years as bandwidth pressures continue to push devices to ever higher frequencies.

1.3 THz Filters

THz filters, on the other hand, are in their infancy and are by and large restricted to periodic structures that provide sharp resonant peaks at desired frequencies [14]. These resonant peaks can be shifted and broadened, but it is difficult to use periodic structures for bandpass filters that are optimally flat over a given frequency range. The bulk of the band pass filters designed in this frequency range are based on patterning subwavelength cross structures onto different materials [15-19]. There have been efforts to create tunable THz filters using dispersive media to spatially spread out the frequency components of broadband pulses and then spatially filter out the unwanted components

[20]. While this approach is interesting, it is unclear that it can provide filter designers with the pass band flatness required for many communication applications.

These various filters are very similar to a traditional enhanced optical transmission device. In these devices, certain frequencies pass through the device at levels higher than what would classically be expected [21]. The frequencies for which the transmission is greater than what is classically expected were found to be dependent on the periodic spacing of the holes in the array. Other factors such as the hole shape, hole size, metal used, and metal thickness have been explored along with the periodicity of the array to determine how light is transmitted through these structures [22]. In addition to experimental research on the geometrical effects of hole arrays, much work has been done on theoretical models for the EOT process [23].

1.4 Enhanced Optical Transmission

Enhanced Optical Transmission (EOT) trough metallic hole arrays has been a well-studied area of physics and optics for the past 14 years. Starting with Thomas Ebbesen, who opened the field with his 1998 paper, “Extraordinary Optical Transmission Through Sub-wavelength Hole Arrays” [24]. Ebbesen discovered that metallic films which are perforated with periodic small holes can exhibit high optical transmission at certain frequencies where the hole size is smaller than the wavelength of incoming light. Researchers have explored this optical phenomenon at great length and a large variety of different structures which employ EOT have been designed, simulated, constructed, and characterized [22]. This work aims to contribute to the considerable work that has been

done in EOT research at the application level, through the development of optical filters at THz frequencies.

The underlying physical process responsible for EOT is believed to arise from incident light that would normally be reflected off a metallic film which is instead coupled to a surface plasmon polariton (SPP) which then propagates along the metal dielectric boundary and is eventually radiated through coupling to the holes in the metal film. Surface plasmons are oscillations in the "sea" of electrons that exist in the conduction band of a metal that occur when excited by the electric field of radiant photons. Due to the nature of the surface plasmon polaritons, incident light cannot directly couple with the surface wave modes. Instead, a wavelength matching mechanism must be used to ensure that the incident photons' momentum is conserved as energy is coupled to the surface wave. This can be accomplished in two main ways through the use of a prism or a scattering mechanism to achieve wavelength matching [25].

If a scattering mechanism is employed, the structure of the scattering material can be engineered to shape the spectrum of the EOT light. Traditional hole arrays have spectra that are related to the periodicity of the perforated holes in the metal film [21]. Our group has shown that by specifying the underlying structure factor of the metal film, the resonant peaks of the transmission spectrum can be engineered to occur at very specific frequencies [26]. This approach allows one to design an ideal filter in the spatial frequency domain and then transform that filter into a physical hole array with EOT spectra matching the desired frequency response. A different approach has shown that manipulating the physical resonant structure of a EOT device can be used to shape the

resulting transmission spectrum [27]. Their approach allows active control over the filter to change the location of resonant peaks in real time.

This work seeks to broaden the functional ability of these EOT filters. Ideally, one would like the ability to create an arbitrary transmission spectrum that is not confined only to the placement of resonant peaks. This would allow the design of low pass, band pass, high pass, and notch filters with good control over the bandwidths of each filter. This may require a fundamental change in the approach to creating EOT filters. This is because many of the desired filter types are based on circles or a superposition of circular structures in the spatial frequency domain; this in turn yields Bessel functions in the spatial domain. The construction of a hole array that is spatially amplitude encoded with a Bessel function is nontrivial and cannot fully follow the shape of a Bessel function due to the binary nature of a hole arrays.

Problems also arise in traditional hole arrays in trying to manipulate the magnitude of individual resonant peaks. Traditional hole arrays are periodic and thus, the frequency response of these devices is a comb in the frequency domain. Often in comb filter design, it is desirable to adjust the magnitudes of the individual frequency components in the comb. Control over each frequency component in a filter enables system designers to perform essential functions such as channel equalization in communication systems, where different frequencies in a signal will be attenuated differently due to the environment. In a traditional hole array, the hole size can have a strong effect on the loss of each frequency component in the resultant comb filter. Thus, researchers have to be very careful when designing a hole array to match the hole size to frequency components of interest. If the hole size matching is done improperly, the

performance of the hole array filter will suffer greatly. This places constraints on the kinds of filters that can be created by traditional hole arrays and on the filter equalization for both periodic and quasi-periodic devices

To overcome this problem, this work seeks to create an EOT filter with gray scale control of the spatial amplitude transmittance. This will allow for the realization of filters with arbitrary frequency responses. To achieve grey scale control of the amplitude transmittance, silver ink is employed to allow spatial control of the conductivity for the EOT filter. By varying the amount of silver printed onto a translucent substrate, the conductivity seen by the propagating SPPs can be controlled. This in turn changes how incident light is coupled and then transmitted through the filter, allowing for complete control over the transmission spectrum.

1.5 References

[1] M. Tonouchi, "Cutting-edge terahertz technology," *Nat. Photonics*, vol. 1, no. 2, pp. 97–105, Feb. 2007.

[2] R. M. Woodward, V. P. Wallace, R. J. Pye, B. E. Cole, D. D. Arnone, E. H. Linfield, and M. Pepper, "Terahertz Pulse Imaging of ex vivo Basal Cell Carcinoma," *J. Invest. Dermatol.*, vol. 120, no. 1, pp. 72–78, Jan. 2003.

[3] Y. C. Shen, T. Lo, P. F. Taday, B. E. Cole, W. R. Tribe, and M. C. Kemp, "Detection and identification of explosives using terahertz pulsed spectroscopic imaging," *Appl. Phys. Lett.*, vol. 86, no. 24, p. 241116, Jun. 2005.

[4] J. F. Federici, B. Schulkin, F. Huang, D. Gary, R. Barat, F. Oliveira, and D. Zimdars, "THz imaging and sensing for security applications—explosives, weapons and drugs," *Semicond. Sci. Technol.*, vol. 20, no. 7, pp. S266–S280, Jul. 2005.

[5] J. Federici and L. Moeller, "Review of terahertz and subterahertz wireless communications," *J. Appl. Phys.*, vol. 107, pp. 111101–22, January 6.

[6] T. Kürner, "Towards Future THz Communications Systems," *Terahertz Sci. Technol. IEEE Trans. On*, vol. 5, Mar. 2012.

[7] S. Cherry, “Edholm’s law of bandwidth,” *Spectr. IEEE*, vol. 41, pp. 58–60, 2004.

[8] “Infineon Introduces SiGe Transceiver Family for Millimeter Wave Wireless Backhaul; Single-Chip ICs Simplify Design of Small Cell Backhaul Links.”

[9] S. Chia, M. Gasparroni, and P. Brick, “The next challenge for cellular networks: backhaul,” *Microw. Mag. IEEE*, vol. 10, pp. 54–66, 2009.

[10] “Radio Spectrum Allocation,” http://transition.fcc.gov/oet/spectrum/table/fcctable.pdf.

[11] B. S. Williams, “Terahertz quantum-cascade lasers,” *Nat Photon*, vol. 1, pp. 517–525, print 2007.

[12] J. T. Darrow, X.-C. Zhang, D. H. Auston, and J. D. Morse, “Saturation properties of large-aperture photoconducting antennas,” *IEEE J. Quantum Electron.*, vol. 28, no. 6, pp. 1607–1616, Jun. 1992.

[13] A. Nahata, A. S. Weling, and T. F. Heinz, “A wideband coherent terahertz spectroscopy system using optical rectification and electro-optic sampling,” *Appl. Phys. Lett.*, vol. 69, no. 16, pp. 2321–2323, Oct. 1996.

[14] J. K. So, M. A. Seo, D. S. Kim, J. H. Kim, S. S. Chang, J.-H. Son, and G.-S. Park, “THz Multi-frequency resonance filter,” in *33rd International Conference on Infrared, Millimeter and Terahertz Waves, 2008. IRMMW-THz 2008*, 2008, pp. 1–1.

[15] A. M. Melo, A. L. Gobbi, M. H. O. Piazzetta, and A. M. P. A. da Silva, “Cross-Shaped Terahertz Metal Mesh Filters: Historical Review and Results,” *Adv. Opt. Technol.*, vol. 2012, May 2012.

[16] O. Paul, R. Beigang, and M. Rahm, “Highly selective terahertz bandpass filters based on trapped mode excitation,” *Opt Express*, vol. 17, pp. 18590–18595, December 10.

[17] L. Mingzhi, L. Wenzao, and E. R. Brown, “High-order THz bandpass filters achieved by multilayer complementary metamaterial structures,” presented at the Infrared Millimeter and Terahertz Waves (IRMMW-THz), 2010 35th International Conference on, 2010, pp. 1–2.

[18] A. M. Melo, M. A. Kornberg, P. Kaufmann, M. H. Piazzetta, E. C. Bortolucci, M. B. Zakia, O. H. Bauer, A. Poglitsch, and A. M. P. Alves da Silva, “Metal mesh resonant filters for terahertz frequencies,” *Appl. Opt.*, vol. 47, no. 32, pp. 6064–6069, Nov. 2008.

[19] D. W. Porterfield, J. L. Hesler, R. Densing, E. R. Mueller, T. W. Crowe, and R. M. Weikle Ii, “Resonant metal-mesh bandpass filters for the far infrared,” *Appl Opt*, vol. 33, pp. 6046–6052, January 9.

[20] R. Mendis, A. Nag, F. Chen, and D. M. Mittleman, "A tunable universal THz filter using artificial dielectrics," presented at the Infrared Millimeter and Terahertz Waves (IRMMW-THz), 2010 35th International Conference on, 2010, pp. 1–2.

[21] J. Gómez Rivas, C. Schotsch, P. Haring Bolivar, and H. Kurz, "Enhanced transmission of THz radiation through subwavelength holes," *Phys. Rev. B*, vol. 68, no. 20, p. 201306, Nov. 2003.

[22] F. J. Garcia-Vidal, L. Martin-Moreno, T. W. Ebbesen, and L. Kuipers, "Light passing through subwavelength apertures," *Rev. Mod. Phys.*, vol. 82, no. 1, pp. 729–787, Mar. 2010.

[23] L. Martín-Moreno, F. J. García-Vidal, H. J. Lezec, K. M. Pellerin, T. Thio, J. B. Pendry, and T. W. Ebbesen, "Theory of Extraordinary Optical Transmission through Subwavelength Hole Arrays," *Phys. Rev. Lett.*, vol. 86, no. 6, pp. 1114–1117, Feb. 2001.

[24] T. W. Ebbesen, H. J. Lezec, H. F. Ghaemi, T. Thio, and P. A. Wolff, "Extraordinary optical transmission through sub-wavelength hole arrays," *Nature*, vol. 391, pp. 667–669, print 1998.

[25] D. Sarid and W. Challener, *Modern Introduction to Surface Plasmons: Theory, Mathematica Modeling, and Applications*. Cambridge University Press, 2010.

[26] T. Matsui, A. Agrawal, A. Nahata, and Z. V. Vardeny, "Transmission resonances through aperiodic arrays of subwavelength apertures," *Nature*, vol. 446, no. 7135, pp. 517–521, Mar. 2007.

[27] H.-T. Chen, W. J. Padilla, J. M. O. Zide, A. C. Gossard, A. J. Taylor, and R. D. Averitt, "Active terahertz metamaterial devices," *Nature*, vol. 444, no. 7119, pp. 597–600, Nov. 2006.

CHAPTER 2

THEORY

This chapter provides a mathematic basis for understanding how the underlying physics of plasmonic filters operate. Starting from Maxwell's equation, a derivation is given for the existence of propagating surface plasmons at a metal/dielectric interface. The dielectric property of a given metal is then incorporated into the propagation of bound surface plasmons by using a derived Drude model. Finally, a derivation of the propagation constant in a cylindrical waveguide is given as it pertains to the transmission behavior of hole array filters. Much of the derivation given in this chapter can be found in a work by Charid and Challener [1] as well as the text by Pozar [2].

2.1 Existence of Surface Plasmons

Working towards an understanding of bound surface plasmon at a metal/dielectric interface, we start with Maxwell's equations.

$$\nabla \times E + \frac{\partial B}{\partial t} = 0 \tag{2.1a}$$

$$\nabla \times H - \frac{\partial D}{\partial t} = j \tag{2.1b}$$

$$\nabla \cdot D = \rho \tag{2.1c}$$

$$\nabla \cdot B = 0 \tag{2.1d}$$

and the constitutive relations:

$$D = \varepsilon E \tag{2.2a}$$

$$B = \mu H \tag{2.2b}$$

$$j = \sigma E \tag{2.2c}$$

assume time harmonic fields for E, D, H, and B of the form:

$$F = F_0 e^{i(k\cdot r - \omega t)} \tag{2.3}$$

where k is the complex wavevector

$$k = k_x\hat{x} + k_y\hat{y} + k_z\hat{z} \tag{2.3}$$

Assuming a homogeneous material free of external current or charge, equation 2.1a and 2.1b become

$$\nabla \times E + j\omega\mu H = 0 \tag{2.4a}$$

$$\nabla \times H - j\omega\varepsilon E = 0 \tag{2.4b}$$

which can be expanded to:

$$\nabla \times E = \begin{vmatrix} \hat{x} & \hat{y} & \hat{z} \\ \frac{\partial}{\partial x} & \frac{\partial}{\partial y} & \frac{\partial}{\partial z} \\ E_x & E_y & E_z \end{vmatrix} = -j\omega\mu H \tag{2.5}$$

Solving for the components of H yields:

$$\mathrm{H}_x = \frac{j}{\omega\mu}\left(\frac{\partial}{\partial y}\mathrm{E}_z - \frac{\partial}{\partial z}\mathrm{E}_y\right) \tag{2.6a}$$

$$\mathrm{H}_y = \frac{j}{\omega\mu}\left(\frac{\partial}{\partial x}\mathrm{E}_z - \frac{\partial}{\partial z}\mathrm{E}_x\right) \tag{2.6b}$$

$$\mathrm{H}_z = \frac{j}{\omega\mu}\left(\frac{\partial}{\partial x}\mathrm{E}_y - \frac{\partial}{\partial y}\mathrm{E}_x\right) \tag{2.6c}$$

Similarly the components of E can be solved from equation 2.4b

$$\mathrm{E}_x = \frac{-j}{\omega\varepsilon}\left(\frac{\partial}{\partial y}\mathrm{H}_z - \frac{\partial}{\partial z}\mathrm{H}_y\right) \tag{2.7a}$$

$$\mathrm{E}_y = \frac{-j}{\omega\varepsilon}\left(\frac{\partial}{\partial x}H_z - \frac{\partial}{\partial z}\mathrm{H}_x\right) \tag{2.7b}$$

$$\mathrm{E}_z = \frac{-j}{\omega\varepsilon}\left(\frac{\partial}{\partial x}\mathrm{H}_y - \frac{\partial}{\partial y}\mathrm{H}_x\right) \tag{2.7c}$$

A propagating TEM wave can be found by manipulating equation 2.4a

$$\nabla \times \nabla \times E = -j\omega\mu\, \nabla \times H \tag{2.8}$$

$$\nabla \times \nabla \times E = \omega^2 \varepsilon\mu\, \mathrm{E} \tag{2.9}$$

Using a Vector Calculus Identity gives

$$\nabla \times \nabla \times E = \nabla(\nabla \cdot \mathrm{E}) - \nabla^2 E \tag{2.10}$$

which in a medium without external charge density simplifies to

$$\nabla \times \nabla \times E = -\nabla^2 E \tag{2.11}$$

yielding the familiar electromagnetic wave equation

$$\nabla^2 E + \omega^2 \varepsilon\mu\, \mathrm{E} = 0 \tag{2.12}$$

which has the well-known solution

$$\mathrm{E} = \mathrm{E}_0 e^{i(nk_0\hat{k} - \omega t)} \tag{2.13}$$

$$\text{where } n = \sqrt{\varepsilon_r \mu_r}, \text{ and } k_0 = \frac{2\pi}{\lambda} \tag{2.14}$$

Now that we have solutions for a propagating wave as well as relationships between the components of the electric and magnetic fields, we can apply these equations to a specific material system. Let us assume a metal and air interface lying in the yz-plane as shown in Fig. 2.1. The metal has permittivity and permeability ε_m , μ_m, respectively, likewise for air ε_a , μ_a.

Further let us assume a TM-polarized mode of propagation along the metal/air interface in the +z direction, polarized along the y-axis. Of the form of equation 2.3, dropping the time dependence

$$\mathrm{H}_x = 0\,, \mathrm{H}_y = \mathrm{A}e^{i(k_x x + k_z z)}, \mathrm{H}_z = 0 \tag{2.15}$$

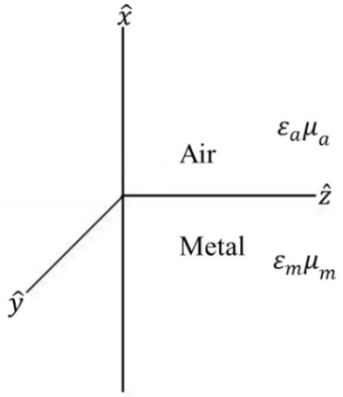

Fig. 2.1. Depiction of a metal/air interface in yz-plane. The permittivity and permeability of the metal are given as ε_m and μ_m, respectively. Likewise for the permittivity and permeability of air ε_a and μ_a.

Propagation along the z direction is characterized by a propagation constant β, propagation into the air and metal is given by γ and δ, respectively, such that

$$k_z = k_0\beta \tag{2.16}$$

$$\gamma^2 = \beta^2 - \varepsilon_a\,\mu_a \tag{2.17}$$

$$\delta^2 = \beta^2 - \varepsilon_m\,\mu_m \tag{2.18}$$

The harmonic magnetic field in the two regions is thus given by

$$\mathrm{H}_y = \mathrm{A}e^{ik_0\beta z}e^{-k_0\gamma x} \quad \text{for } x > 0 \tag{2.19a}$$

$$\mathrm{H}_y = \mathrm{A}e^{ik_0\beta z} \quad \text{for } x = 0 \tag{2.19b}$$

$$\mathrm{H}_y = \mathrm{A}e^{ik_0\beta z}e^{k_0\delta x} \quad \text{for } x < 0 \tag{2.19c}$$

which decays exponentially away from the interface into the air and metal. Applying equations 2.7a to the above expression show only two non-zero contributions exist for the electric field, E_x and E_z

$$\mathrm{E}_x = \frac{j}{\omega\varepsilon}\frac{\partial}{\partial z}\mathrm{H}_y \tag{2.20a}$$

$$\mathrm{E}_x = \begin{bmatrix} -A\dfrac{k_0\beta}{\omega\varepsilon_0\varepsilon_a}e^{ik_0\beta z}e^{-k_0\gamma x} & \text{for } x > 0 \\ -A\dfrac{k_0\beta}{\omega\varepsilon_0\varepsilon_m}e^{ik_0\beta z}e^{k_0\delta x} & \text{for } x < 0 \end{bmatrix} \tag{2.21a}$$

$$\mathrm{E}_z = \frac{-j}{\omega\varepsilon}\frac{\partial}{\partial x}\mathrm{H}_y \tag{2.20b}$$

$$\mathrm{E}_z = \begin{bmatrix} A\frac{jk_0\gamma}{\omega\varepsilon_0\varepsilon_a}e^{ik_0\beta z}e^{-k_0\gamma x} & \text{for } x > 0 \\ -A\frac{jk_0\delta}{\omega\varepsilon_0\varepsilon_m}e^{ik_0\beta z}e^{k_0\delta x} & \text{for } x < 0 \end{bmatrix} \tag{2.21b}$$

The electric field components are also seen to decay exponentially away from the interface. The only propagating fields occur at the interface of the air/metal system, thus demonstrating a true bound surface wave with propagation constant β. To determine the propagation constant, we must apply the appropriate boundary conditions based on the material system. Because we have assumed TM polarized radiation along the y direction, only the electric field need be constant across the interface, as stated below.

$$\hat{n}_{am} \times (E_m - E_a) = 0 \tag{2.22}$$

Here, $\hat{n}_{am}$ is the unit vector pointing normal to the air/metal interface. Thus, the E_z component must match across the boundary, yielding the relation

$$\frac{\gamma}{\varepsilon_a} = \frac{-\delta}{\varepsilon_m} \tag{2.23}$$

Substituting in β gives

$$\frac{\beta^2 - \varepsilon_a\mu_a}{{\varepsilon_a}^2} = \frac{\beta^2 - \varepsilon_m\mu_m}{{\varepsilon_m}^2} \tag{2.24}$$

$${\varepsilon_m}^2\beta^2 - \varepsilon_a\mu_a{\varepsilon_m}^2 = {\varepsilon_a}^2\beta^2 - \varepsilon_m\mu_m{\varepsilon_a}^2 \tag{2.25}$$

$$\beta = \sqrt{\frac{\varepsilon_a\mu_a{\varepsilon_m}^2 - \varepsilon_m\mu_m{\varepsilon_a}^2}{{\varepsilon_m}^2 - {\varepsilon_a}^2}} \tag{2.26}$$

$$\beta = \sqrt{\frac{\varepsilon_a\varepsilon_m(\mu_a\varepsilon_m - \mu_m\varepsilon_a)}{(\varepsilon_m + \varepsilon_a)(\varepsilon_m - \varepsilon_a)}} \tag{2.27}$$

Assume μ_a and μ_m are equal to 1; the metal is not ferromagnetic, nor is air

$$\beta = \sqrt{\frac{\varepsilon_a\varepsilon_m}{\varepsilon_m + \varepsilon_a}} \tag{2.28}$$

Air in this system could easily be replaced by another dielectric, and thus, $\varepsilon_a$could be some other ε_d; we will round ε_a to be exactly 1

$$\beta = \sqrt{\frac{\varepsilon_m}{\varepsilon_m+1}} \tag{2.29}$$

The real part of the dielectric constant of a metal is negative below its plasma frequency (to be explained later); consequentially, the propagation constant for a bound surface wave propagating along the surface of a metal\dielectric boundary will always be greater than one. Such an electromagnetic wave is termed a Surface Plasmon Polariton (SPP). Because the propagation constant for the bound wave is greater than one, the wavevector, given by $k_z = k_0\beta$, will always be greater than the wavevector of freely propagating electromagnetic radiation, k_0. This mismatch in wavevectors means that freely propagating radiation cannot directly couple to bound SPP modes. To efficiently couple radiation into the bound surface modes requires a momentum matching scheme, to transfer energy from one wavevector to the other. Various mechanisms have been shown to provide this matching, such as prisms, gratings, and sufficient surface roughness; whatever the mechanism, it must satisfy the basic equation:

$$k_{spp} = k_0 + k_{match} \tag{2.30}$$

2.2 Drude Model of Metals

To determine what k_{spp} is for a metal dielectric interface over a given frequency range, $\varepsilon_m(\omega)$ must be determined. Using the Drude model of a free electron gas, we can use a classical approach to find dielectric function of a metal substrate. This classical approach treats a free electron in the metal as a harmonic oscillator, which is then forced

by an impinging electric field. The impinging electric field $\vec{E}$ displaces the electron by a distance r, creating a dipole moment, $\vec{u}$.

$$\vec{u} = e\vec{r}, \tag{2.31}$$

e is the charge on an electron; the electric displacement field $\vec{D}$ is given by

$$\vec{D} = \varepsilon_0\vec{E} + \vec{P} \tag{2.32}$$

$\vec{P}$ is the polarization density field within the metal, which is related to the dipole moment and the number or electrons in the metal.

$\vec{P} = n\vec{u}$, where n is the number or electrons in the metal, thus

$$\vec{D} = \varepsilon_0\vec{E} + n\vec{u} \tag{2.33}$$

and from the constitutive relation of 2.2a

$$\vec{E}\varepsilon_0\varepsilon_m = \varepsilon_0\vec{E} + ne\vec{r} \tag{2.34}$$

$$\varepsilon_m = 1 + \frac{|\vec{P}|}{|\varepsilon_0\vec{E}|} \tag{2.35}$$

The polarization density field can be found in terms of $\vec{E}$ if the position of the electron can be solved it terms of $\vec{E}$. Here, the harmonic equation of motion for the electron is assumed.

$$m_e\frac{\partial^2 r}{\partial t^2} + \Gamma\frac{\partial r}{\partial t} = e\left|\vec{E}\right|e^{-j\omega t} \tag{2.36}$$

where Γ, the damping of the electron, is related to the Fermi velocity and mean free path of the electron. $m_e$is the mass of the electron. Assume a harmonic solution to the above equation, which will follow the forcing field.

$$r(t) = Ce^{-j\omega t} \tag{2.37}$$

To find the constant, C, we will insert the proposed solution into equation 2.36

$$-m_eC^2\omega^2e^{-j\omega t} - m_eCj\omega\Gamma e^{-j\omega t} = e\left|\vec{E}\right|e^{-j\omega t} \tag{2.38}$$

Isolating C

$$C = \frac{-e|\vec{E}|}{m_e(\omega^2 + j\omega\Gamma)}\,,\; r(t) = \frac{-e|\vec{E}|}{m_e(\omega^2 + j\omega\Gamma)}\,e^{-j\omega t} \tag{2.39}$$

Using this result with equations 2.35 gives the Drude model of the dielectric function for a metal

$$\varepsilon_m = 1 - \frac{ne\left(\frac{(e\vec{E})}{m_e(\omega^2 + j\omega\Gamma)}\right)}{|\varepsilon_0\vec{E}|} \tag{2.40}$$

which can be simplified to

$$\varepsilon_m = 1 - \frac{{\omega_p}^2}{(\omega^2 + j\omega\Gamma)} \tag{2.41}$$

where

$$\omega_p = \sqrt{\frac{ne^2}{\varepsilon_0 m_e}} \tag{2.42}$$

The real part of the dielectric function of a metal is seen to have a transition from negative values to positive values at the plasma frequency of the metal, ω_p. The final expression for the wavenumber of a propagating surface plasmon on an air/metal interface is given below.

$$\beta = \sqrt{\frac{1 - \frac{{\omega_p}^2}{(\omega^2 + j\omega\Gamma)}}{2 - \frac{{\omega_p}^2}{(\omega^2 + j\omega\Gamma)}}} \tag{2.43}$$

One way to satisfy equation 2.30, the momentum matching required to couple to surface plasmon modes, is to create an arrayed structure where the periodic nature of the structure creates a well-defined k-vector, such as in a grating. Metal films with a periodic array of perforated holes, termed a Hole Array (HA), possess the required k-vector matching and can be seen to be similar to a traditional grating.

$$k_{spp} = k_0 + k_{grating} \tag{2.44}$$

or equivalently

$$k_{spp} = k_0 + k_{HA} \tag{2.45}$$

2.3 Cylindrical Waveguides

Hole arrays have been experimentally demonstrated to support SPP propagation and satisfy the above equation. The effect of hole shape, size, and depth on surface plasmon propagation have also been thoroughly investigated [3]. Using theory, the effect of a single hole can be examined. The effect on hole size in traditional hole arrays can be found by treating the perforated metal film as circular waveguide. A depiction of circular waveguide is shown in Fig. 2.2 both cylindrical and rectangular coordinates. The propagating solution to the waveguide can be found by again employing Maxwell's equations, but this time in cylindrical coordinates paralleling equations 2.6 and 2.7, as shown below.

$$\mathrm{H}_\rho = \frac{j}{{k_c}^2}\left(\frac{\omega\varepsilon}{\rho}\frac{\partial}{\partial\phi}\mathrm{E}_z - \beta\frac{\partial}{\partial\rho}\mathrm{H}_z\right) \tag{2.46a}$$

$$\mathrm{H}_\phi = \frac{-j}{{k_c}^2}\left(\omega\varepsilon\frac{\partial}{\partial\rho}\mathrm{E}_z + \frac{\beta}{\rho}\frac{\partial}{\partial\phi}\mathrm{H}_z\right) \tag{2.46b}$$

$$\mathrm{E}_\rho = \frac{-j}{{k_c}^2}\left(\beta\frac{\partial}{\partial\rho}\mathrm{E}_z + \frac{\omega\varepsilon}{\rho}\frac{\partial}{\partial\rho}\mathrm{H}_z\right) \tag{2.46c}$$

$$\mathrm{E}_\phi = \frac{j}{{k_c}^2}\left(\frac{\beta}{\rho}\frac{\partial}{\partial\phi}\mathrm{E}_z - \omega\varepsilon\frac{\partial}{\partial\rho}\mathrm{H}_z\right) \tag{2.46d}$$

$$\text{Here: } {k_c}^2 = {k_0}^2 - \beta^2, \tag{2.47}$$

k_c is the cut off wavenumber for the waveguide. Let us again assume a TM polarized mode through the waveguide, where $H_z = 0$ and E_z must obey the equation of 2.12.

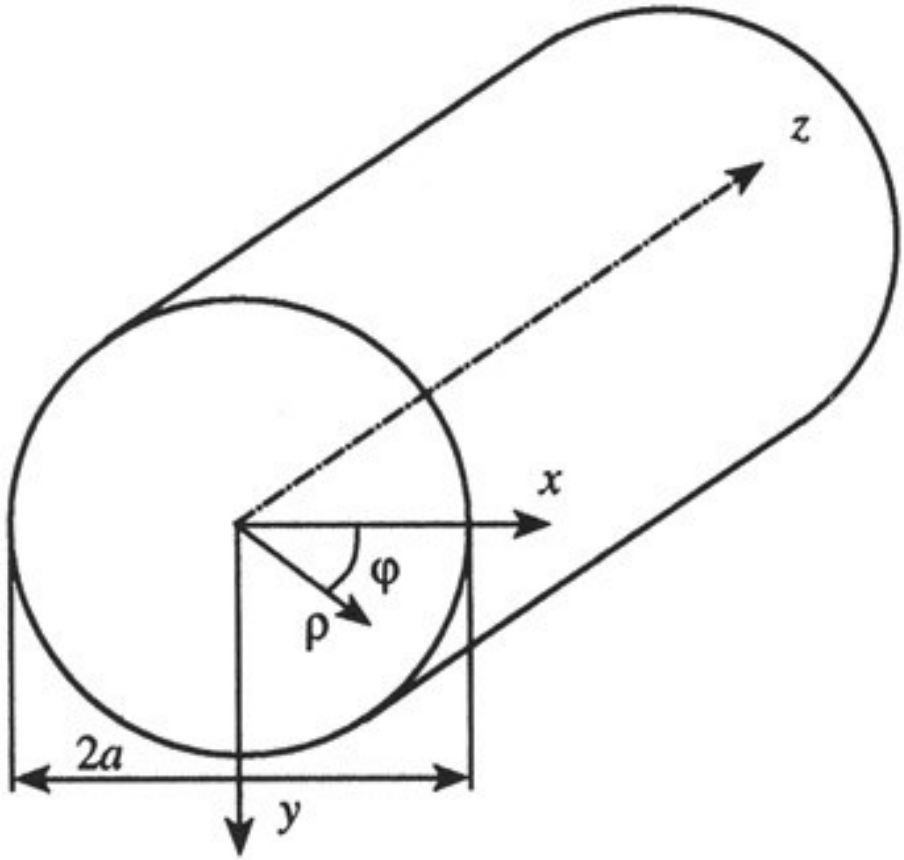

Fig. 2.2. Depiction of a cylindrical waveguide with the long axis oriented along the z-axis. The waveguide has a radius of a.

$$\nabla^2 \mathrm{E}_z + k^2 \mathrm{E}_z = 0 \tag{2.48}$$

which in cylindrical coordinates takes the following form

$$\left(\frac{\partial^2}{\partial \rho^2} + \frac{1}{\rho}\frac{\partial}{\partial \rho} + \frac{1}{\rho^2}\frac{\partial^2}{\partial \phi^2} + {k_c}^2\right)\mathrm{E}_z = 0 \tag{2.49}$$

To find solutions for E_z, we employ the separation of variables technique

$$R(\rho)P(\phi) = \mathrm{E}_z \tag{2.50}$$

$$P\frac{\partial^2 R}{\partial \rho^2} + P\frac{1}{\rho}\frac{\partial R}{\partial \rho} + \frac{R}{\rho^2}\frac{\partial^2 P}{\partial \phi^2} + RP{k_c}^2 = 0 \tag{2.51}$$

Divide by $R(\rho)$ and $P(\phi)$

$$\frac{1}{R}\frac{\partial^2 R}{\partial \rho^2} + \frac{1}{R}\frac{1}{\rho}\frac{\partial R}{\partial \rho} + \frac{1}{P}\frac{1}{\rho^2}\frac{\partial^2 P}{\partial \phi^2} + {k_c}^2 = 0 \tag{2.52}$$

Multiply by $\rho^2$and separate $R(\rho)$ and $P(\phi)$

$$\frac{\rho^2}{R}\frac{\partial^2 R}{\partial \rho^2}+\frac{\rho}{R}\frac{\partial R}{\partial \rho}+\rho^2 {k_c}^2=-\frac{1}{P}\frac{\partial^2 P}{\partial \phi^2} \tag{2.53}$$

The two sides of the equation are independent of each other; the LHS is dependent only on ρ and the RHS is dependent only on ϕ. Because the two sides are independent of each other, they can be solved separately and set equal to a common constant m^2. Starting with the RHS:

$$m^2=-\frac{1}{P}\frac{\partial^2 P}{\partial \phi^2} \tag{2.54}$$

$$m^2 P+\frac{\partial^2 P}{\partial \phi^2}=0 \tag{2.55}$$

The solution to this simple second order differential equation is the well-known superposition of periodic functions sine and cosine.

$$P(\phi)=A\sin m\phi+B\cos m\phi \tag{2.56}$$

The LHS of the equation is then Bessel's differential equation:

$$\rho^2\frac{\partial^2 R}{\partial \rho^2}+\rho\frac{\partial R}{\partial \rho}+R\left(\rho^2 {k_c}^2-m^2\right)=0 \tag{2.57}$$

with solutions of Bessel functions given by:

$$R(\rho)=C\cdot J_n(k_c\rho)+D\cdot Y_n(k_c\rho) \tag{2.58}$$

The bessel function of the second kind Y_n, is infinite for $\rho=0$, thus $D=0$. The final solution of the electric field E_z for a TM mode propagating is given below

$$\mathrm{E}_z=(A\sin m\phi+B\cos m\phi)J_n(k_c\rho)e^{-i\beta z} \tag{2.59}$$

Once again to find the propagation constant for the field, the boundary conditions from the material system must be applied. Namely that at the conductive walls of the waveguide, the tangential electric field must go to zero.

$E_z(\phi, a) = 0$, where a is the radius of the waveguide

$$J_n(k_c a) = 0 \tag{2.60}$$

Thus we see that the cut-off wavenumber is related to the zeros of a Bessel function and the radius of the waveguide. $k_c a = P_{nm}$, where P_{nm} are the roots of the Bessel function, yielding $k_c = \frac{P_{nm}}{a}$, which can be used to find β, the propagation constant.

$$\beta^2 = {k_0}^2 - {k_c}^2 \tag{2.61}$$

$$\beta = \sqrt{{k_0}^2 - \left(\frac{P_{nm}}{a}\right)^2} \tag{2.62}$$

As can be seen in the above equation, if the wavenumber of radiation exciting the waveguide falls below the cut-off wavenumber, which is determined by the dimension of the waveguide, β will become negative and the fields propagating in the z-direction will become evanescent and will decay exponentially along the waveguide. This cut-off wavenumber has a corresponding cut-off frequency shown below.

$$f_c = \frac{P_{nm}}{2\pi a\sqrt{\varepsilon\mu}} \tag{2.63}$$

This relationship between hole size and propagation constant in cylindrical waveguides can be useful in controlling the transmission properties in metallic hole arrays. This is due to the coupling between free-space radiation, bound surface plasmons, and cylindrical waveguide modes of the perforated hole. As incoming light is incident upon a hole array; radiation is coupled into the surface plasmon in accordance with equation 2.45, the bound surface plasmon is then coupled into the cylindrical waveguide of the holes of the film with a propagation constant given by equation 2.62. This coupling process is then reversed on the opposite side of the hole array emitting certain frequencies of light back into free-space determined by the geometric and material properties of the

hole array. This process is known formerly as Extraordinary Optical Transmission (EOT). The next chapter will show experimentally how changing hole size specifically can affect this EOT process.

2.4 References

[1] D. Sarid and W. Challener, *Modern Introduction to Surface Plasmons: Theory, Mathematica Modeling, and Applications*. Cambridge University Press, 2010.

[2] D. M.Pozar, *Microwave Engineering, 3Rd Ed*. Wiley India Pvt. Limited, 2009.

[3] F. J. Garcia-Vidal, L. Martin-Moreno, T. W. Ebbesen, and L. Kuipers, "Light passing through subwavelength apertures," *Rev. Mod. Phys.*, vol. 82, no. 1, pp. 729–787, Mar. 2010.

[4] A. Agrawal, Z. V. Vardeny, and A. Nahata, "Engineering the dielectric function of plasmonic lattices," *Opt. Express*, vol. 16, no. 13, pp. 9601–9613, Jun. 2008.

[5] T. Matsui, A. Agrawal, A. Nahata, and Z. V. Vardeny, "Transmission resonances through aperiodic arrays of subwavelength apertures," *Nature*, vol. 446, no. 7135, pp. 517–521, Mar. 2007.

[6] D. Grischkowsky, S. Keiding, M. van Exter, and C. Fattinger, "Far-infrared time-domain spectroscopy with terahertz beams of dielectrics and semiconductors," *J. Opt. Soc. Am. B*, vol. 7, no. 10, pp. 2006–2015, Oct. 1990.

CHAPTER 3

STATISTICAL HOLE SIZE VARIATION IN PLASMONIC FILTERS

In this chapter, we demonstrate a THz filter design concept that allows for variable power control of multiple frequencies in an Enhanced Optical Transmission device. The filter is composed of a stainless steel thick film with subwavelength holes patterned into the film to create an underlying structure factor. By statistically controlling the hole sizes in the quasi periodic array, the designer can vary the power coupled to the individual frequency components of the filter. Experimental results show how this design methodology can be used to create frequency weighted filters, and an application for flattening the spectrum of a THz emitter.

3.1 Previous Work

In the previous theory chapter, derivations for surface plasmons, Drude metals, and cylindrical waveguides were given; these different topics were all discussed as they contribute to the response of metallic hole arrays. At the end of the theory section, a brief overview of the effect of hole size on transmission was proposed. The effect of hole size on transmission at THz frequencies has been examined experimentally in previous work by our research group [1]. In this previous work, the transmission

response of a metal film with a random array of perforated round holes was characterized. The effective permittivity of the perforated metal film followed the Drude model for a lossy plasma. In this model, the traditional plasma frequency term ω_p, is replaced by an effective plasma frequency ω_c, given by the cut-off frequency of the cylindrical waveguide of the perforated hole. This cut-off frequency is related to equation 2.63 of the preceding theory section as $\omega_c = c\frac{P_{nm}}{a}$.

The pseudo cut-off plasma frequency determined by the radius of the perforated hole directly affects the effective permittivity of the metal film and thus changes the frequency dependent transmission of the structure. Fig. 3.1, taken from the previous work, shows the transmission response of the random array of holes along with the measured and predicted permittivity of the perforated film [1].

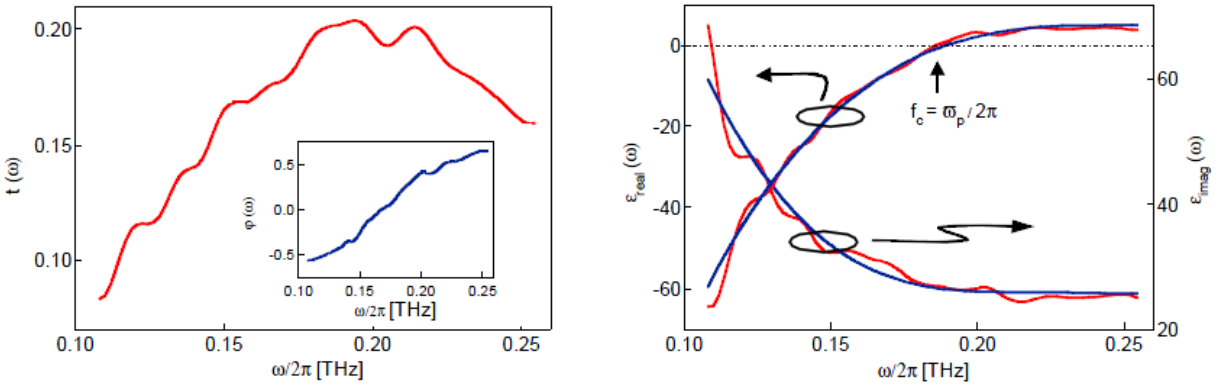

Fig. 3.1. Determination of the real and imaginary components of $\varepsilon(\omega)$ for a random aperture array with D = 800 μm and fractional aperture area of 12%. a) The amplitude transmission, $t(\omega)$ and phase, $\varphi(\omega)$ (Inset) spectra measured using THz-TDS. b) Spectra of real and imaginary $\varepsilon(\omega)$ components (red line) obtained from $t(\omega)$ and $\varphi(\omega)$ shown in (a). $\varepsilon_{real}(\omega)$ is shown to pass through zero value at fc = 0.19 THz.[4]

The good agreement between predicted and measured permittivity supports the altered Drude model, giving a good method for predicting the effect perforate hole size has on extraordinary optical transmission. The results shown in Fig. 3.1 were for an array of random holes, meaning that no structure was applied to the placement of each hole. This allows one to see only the characteristic of a single hole, where the response of the single hole is only scaled by the total number of holes in the randomly placed array. To further validate the developed permittivity model, a periodic array of perforated holes was also characterized. The transmission responses of several periodic hole arrays, arrays with the same period but different sized holes, as well as random hole arrays were also measured for four different sized holes [1]. This allows one to separate the contribution by the structure of the periodic array as well as the contribution from a single perforated hole. The results from this previous work in our group are shown in Fig. 3.2.

As can be seen in Fig. 3.2, the frequency response contains sharp narrow resonances as well as a broadband background. The narrow resonances occur at frequencies corresponding directly to the periodicity of the array and higher order integer modes. The resonant mode frequencies are given by $\omega_R = \frac{2\pi c}{P}\sqrt{m^2 + n^2}$, where P is the period of the structure, m and n are the integer number of modes. While the location of the narrow resonance stays constant across the samples of different sized holes, the background response changes dramatically. Furthermore, the background response of the periodic array is seen to follow closely with the transmission response of the matching random array of holes. This suggests that the narrow resonant contribution from the structured placement of the holes rides on top of the background contribution of the cylindrical waveguide determined by the size of the hole in the array.

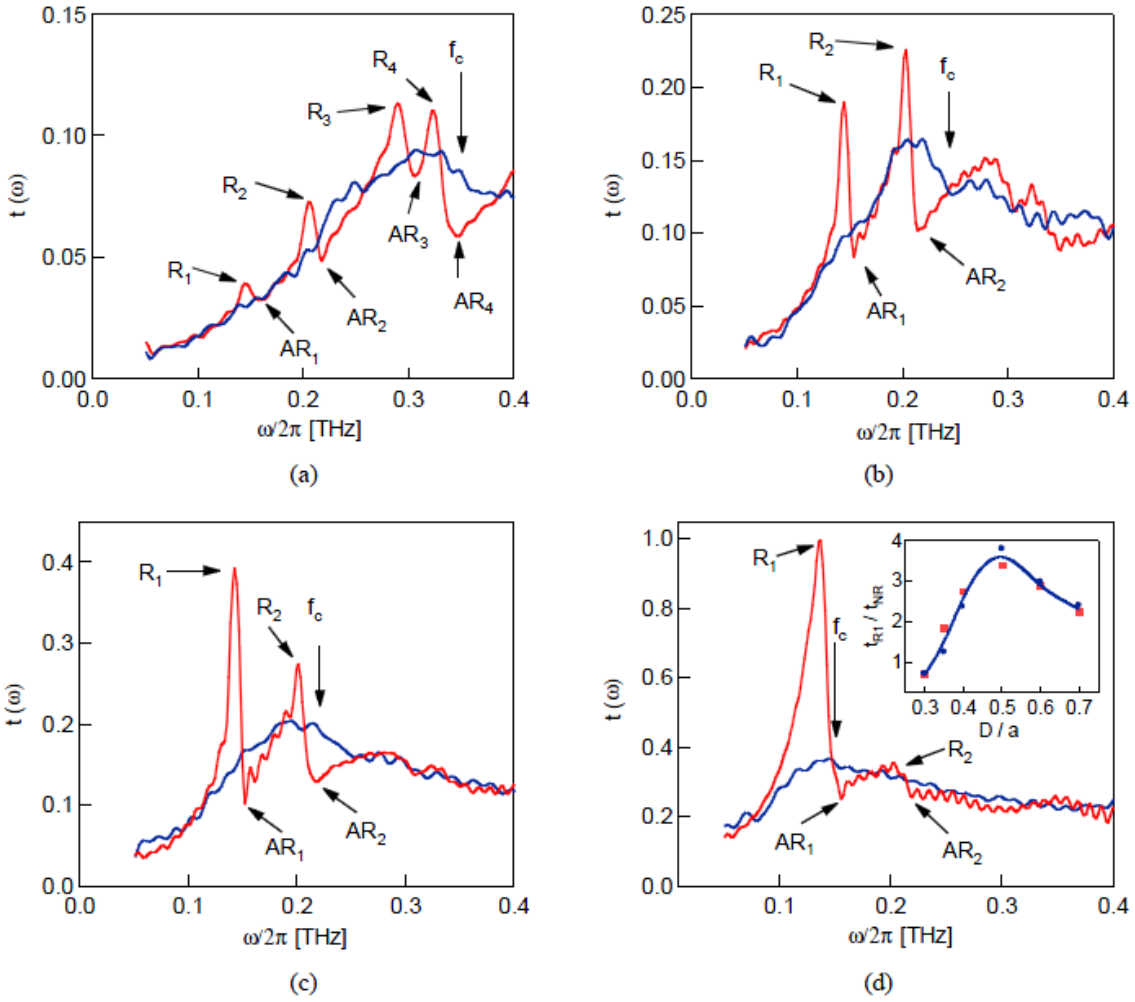

Fig. 3.2. THz-TDS studies of stainless steel foils perforated with periodic (red line) and random (blue line) aperture arrays that were designed to have the same fractional aperture area and aperture diameter D as the corresponding periodic arrays. (a)-(d), $t(\omega)$ spectra for structures with a = 2 mm and (a) D = 500 μm (b) 700 μm (c) 800 μm and (d) 1200 μm. The resonant (R_i) and antiresonant (AR_i) frequencies are assigned, along with the cutoff frequency, fc for the individual apertures. (The inset in (d) is the ratio of the transmittance, t_{R1} at the R1 (±1, 0) resonance in the periodic EOT spectrum, to the peak transmittance, t_{NR} of the nonresonant background in the corresponding random array spectrum, as a function of D/a.[4]

3.2 Statistical Hole Size Approach

Using this previously developed model for hole arrays, the parameters of hole placement and hole size can be used to create frequency selective filters with specific resonant locations, transmission, and quality factor. This type of filter can be used in many applications across the electromagnetic spectrum, from the ultraviolet to the far-infrared THz region, due to the scale invariant properties of Maxwell's equations. Using a variation on strictly periodic array to what is termed a quasi-periodic array of holes has shown promise in offering more flexibility in filter design. This technique will be discussed at greater length in the next section on k-space design. To briefly describe quasi-periodic structures, one places holes in a pattern that has no repeating unit cell, but a certain level of order and symmetry that forms an underlying structure fracture in k-space. This k-space structure factor is determined by taking the two-dimensional Fourier transform of the real space structure. By defining the k-space structure in advance of placing the holes, one can directly specify the frequency response of a desired filter. This approach was demonstrated previously by our group at THz frequencies [2].

To show the filtering advantages of intelligently designed holes in plasmonic quasi-periodic structures, we demonstrate a filter with two distinct resonant peaks whose relative magnitude can be adjusted. To accomplish this, we create a filter with a quasi-periodic structure defined by a k-space transform that has two distinct resonance frequencies. The details of how such a quasi-periodic structure is generated are discussed in the next section. Quasi-periodic hole arrays are similar to strictly periodic hole arrays as they both have resonant behavior dictated by their underlying k-space structure factor [2]. The advantage in using quasi-periodic arrays over traditional periodic arrays comes

in the added flexibility in defining the structure factor for the quasi-periodic hole array. Once a filter structure with the desired resonances has been obtained, a developed thresholding algorithm is used to reduce the greyscale quasi-periodic structure to a set of discrete points. These discrete points represent a rough back bone of the desired structure. The x-y coordinates of each discrete point is then used as the location for a perforated hole, thus creating a quasi-periodic hole array.

By selecting the hole size of each perforated hole in the quasi-periodic array, the slowly varying background frequency response of the filter can be tuned. Smaller sized holes cause the frequency response to be greater at higher frequencies, while larger sized holes shift the background frequency response to lower frequencies, as described in Fig. 3.2. By statistically sorting each hole in the array to be either a large sized or small sized hole, the relative magnitudes of the two resonant frequencies of the filter can be tuned. For instance, if the probability of any given hole being assigned a large radius is increased, the relative magnitude of the lower frequency resonance will increase. Correspondingly, if the probability of a given hole being assigned a small radius is increased, the relative magnitude of the higher frequency resonance will increase. Using this method, the x-y coordinates of each hole in the quasi-periodic array are statistically sorted into one of two bins, one representing small sized holes, the other large sized holes. The probability p, used to sort the holes is adjusted to tune the relative magnitudes of the two resonant frequencies of the filter. Once the filter has been designed with the proper structure and hole sizes, it is fabricated by the laser ablation of stainless steel films. The resultant stainless steel hole arrays are then tested in a traditional THz Time

Domain Spectroscopy system (THz-TDS) [3]. The obtained time domain waveforms are then Fourier transformed to give the measured frequency response of the filter.

3.3 Experimental Results

To demonstrate this design flow, two sets of statistically sized hole array filters are shown in Fig. 3.3 and 3.4. Fig. 3.3 describes a dual resonance filter with a low frequency peak at .25 THz and a high frequency peak at .375 THz. Fig. 3.3a shows the designed k-space structure factor for the filter; the resonances located at $2.6 \times 10^3 \frac{1}{m}$ and $3.9 \times 10^3 \frac{1}{m}$ correspond to .25 THz and .375 THz. Fig. 3.3b depicts the real space structure obtained from a 2D inverse Fourier transform of Fig. 3.3a. The structure is a continuously varying greyscale image; using a custom developed thresholding algorithm, the image is converted into a series of discrete points with x-y coordinates. Fig. 3.3c shows the .25-.375 THz hole array filter statistically weighted for lower frequencies. Fig. 3.3d shows the .25-.375 THz hole array filter statistically weighted for higher frequencies. The assigned large holes are represented by blue **x**'s and the small holes represented by red **o**'s. Fig. 3.3e is the measured THz-TDS transmission response of the filter depicted in Fig. 3.3c from .1 THz to .5 THz. As expected, the lower frequency resonance at .25 THz is clearly greater than the high frequency resonance at .375 THz. Fig. 3.3f is the measured THz-TDS transmission response of the filter depicted in Fig. 3.3d from .1 to .5 THz. Now that the probability weighting is reversed, the lower frequency resonance at .25 THz is smaller than the high frequency resonance at .375 THz.

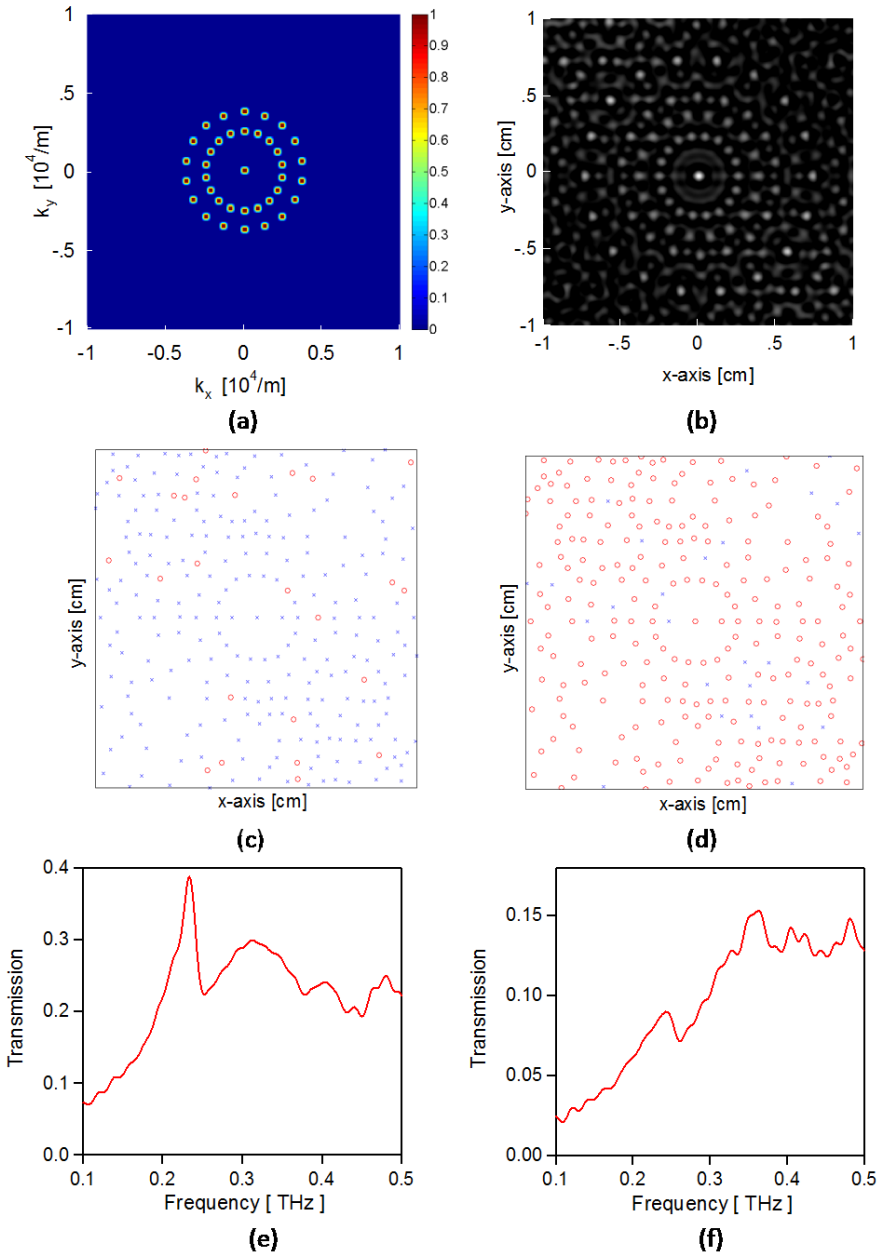

Fig. 3.3 Dual resonance filter with a low frequency peak at .25 THz and a high frequency peak at .375 THz. (a) designed k-space structure factor for the filter; the resonances located at $2.6 \times 10^3 \frac{1}{m}$ and $3.9 \times 10^3 \frac{1}{m}$ correspond to .25 THz and .375 THz. (b) real space structure obtained from a 2D inverse Fourier transform of (a). (c) .25 THz / .375 THz hole array filter with statistical weight $p = .9$ for lower frequencies. The assigned large holes are represented by blue **x**'s and the small holes represented by red **o**'s. (d) .25 THz / .375 THz hole array filter with statistical weight $p = .1$ for lower frequencies. The assigned large holes are represented by blue **x**'s and the small holes represented by red **o**'s. (e) Measured frequency response of the filter depicted in (c). (e) Measured frequency response of the filter depicted in (d).

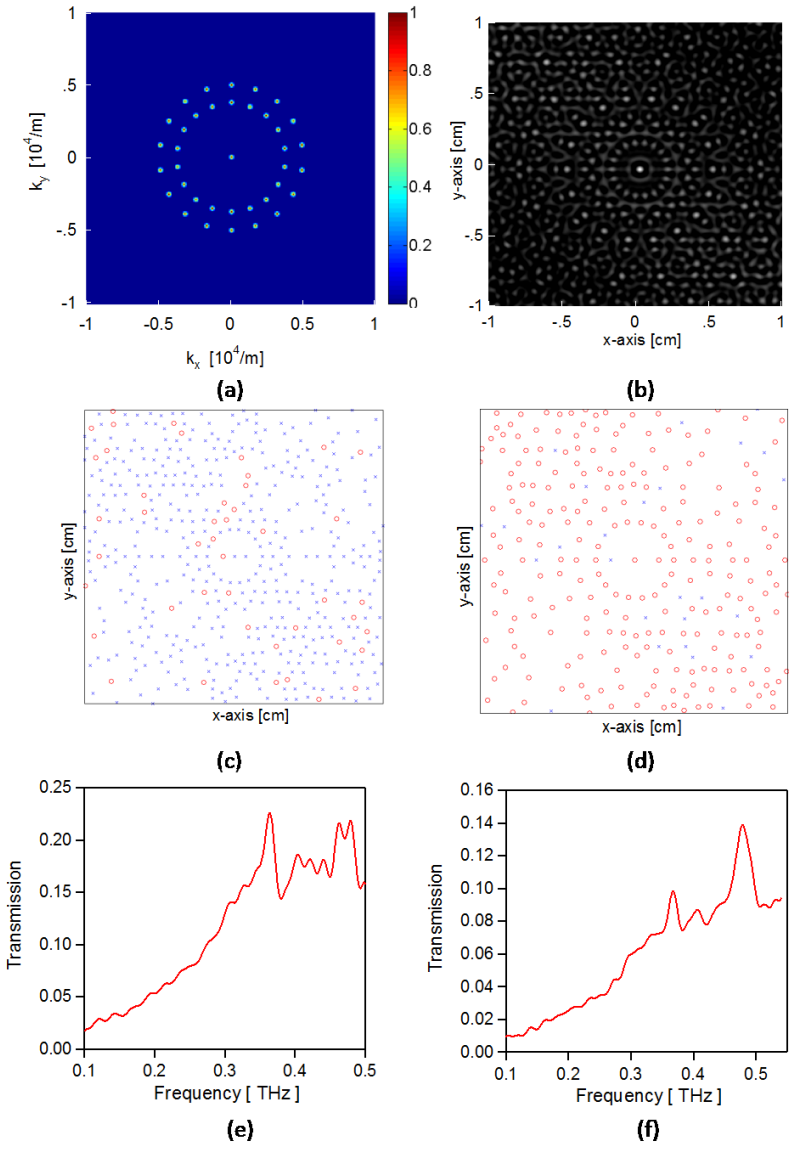

Fig. 3.4 Dual resonance filter with a low frequency peak at .375 THz and a high frequency peak at .5 THz. (a) designed k-space structure factor for the filter; the resonances located at $3.9 \times 10^3 \frac{1}{m}$ and $5.2 \times 10^3 \frac{1}{m}$ correspond to .375 THz and .5 THz. (b) real space structure obtained from a 2D inverse Fourier transform of (a). The structure is a continuously varying greyscale image. (c) .375 THz / .5 THz hole array filter with statistical weight $p = .9$ for lower frequencies. The assigned large holes are represented by blue **x**'s and the small holes represented by red **o**'s. (d) .375 THz / .5 THz hole array filter with statistical weight $p = .1$ for lower frequencies. The assigned large holes are represented by blue **x**'s and the small holes represented by red **o**'s. (e) Measured frequency response of the filter depicted in (c); the .375 THz resonance is clearly higher than the .5 THz resonance. (f) Measured frequency response of the filter depicted in (d), the .5 THz resonance is now higher than the .375 THz resonance.

To further demonstrate the reliability of this method, a second set of filters is presented in Fig. 3.4. The filters are again dual resonant, but with a low frequency resonance at .375 THz and a high frequency resonance at .5 THz. Fig. 3.4 follows the same flow of Fig. 3.3. The results of Fig. 3.3 and Fig. 3.4 show good agreement with the predicted behavior of hole size discussed earlier in Fig. 3.2. These results suggest statistically weighting the hole sizes in a quasi-periodic plasmonic structure is a viable way to tune the frequency response of a filter. Variation of the relative magnitudes of the two resonances in the filter is significant as shown in Fig. 3.3e / Fig. 3.3f and Fig. 3.4e / Fig. 3.4f, allowing for a new degree of control in filter design.

This kind of filtering capability would be required in a THz Frequency Shift Keyed (FSK) communication system where two distinct carrier frequencies are used to transmit information through a wireless channel. Due to frequency selective fading in a physical channel, the carrier frequencies power needs to be equalized at the receiver after propagating through the channel. This works demonstrates a THz filter design methodology that allows variable power transmission control over the individual frequency components of the filter. This new capability helps fill in one of the gaps in a realizable THz FSK system. This filtering approach might also be useful in more fundamental research in allowing one to flatten the output spectrum of a THz emitter.

3.4 References

[1] A. Agrawal, Z. V. Vardeny, and A. Nahata, "Engineering the dielectric function of plasmonic lattices," *Opt. Express*, vol. 16, no. 13, pp. 9601–9613, Jun. 2008.

[2] T. Matsui, A. Agrawal, A. Nahata, and Z. V. Vardeny, "Transmission resonances through aperiodic arrays of subwavelength apertures," *Nature*, vol. 446, no. 7135, pp. 517–521, Mar. 2007.

[3] D. Grischkowsky, S. Keiding, M. van Exter, and C. Fattinger, “Far-infrared time-domain spectroscopy with terahertz beams of dielectrics and semiconductors,” *J. Opt. Soc. Am. B*, vol. 7, no. 10, pp. 2006–2015, Oct. 1990.

CHAPTER 4

K-SPACE DESIGN OF TERAHERTZ PLASMONIC FILTERS

4.1 Motivation

Filter technology is an extremely broad and well-studied field, with numerous applications in science and engineering, from the first power line filters [1], to the advanced digital filters in modern electronics [2,3] and wavelength-division multiplexing filters in fiber optic communication systems [4]. While well-defined filter design methodologies exist for much of the electromagnetic spectrum [5,6], the THz region of the spectrum lags behind in filter complexity and lacks the same caliber of design capabilities. Here, we report a versatile technique for designing different classes of THz plasmonic filters based on a k-space methodology, in which the desired frequency response is mapped into two-dimensional (2D) k-space and then inverse Fourier transformed into the spatial domain. In general, any technique that allows for grey scale variation in the fabricated plasmonic structure, ensuring high fidelity reproduction of the real space pattern, can be used; we use a recently developed inkjet printing technique that allows for grey scale conductivity variation [7]. We demonstrate the flexibility of this approach by creating several classes of filters that allow for changes in the relative magnitudes in multiresonance filters, the polarization dependence, where the anisotropy and the resonance bandwidth can be carefully controlled. We further demonstrate that by

cascading or adding filter functions together, even more complex filter designs can be achieved. We expect this approach to dramatically expand the design capabilities for filter technology for THz systems applications, such as THz wireless communications [8], as well as applications in other spectral regions.

The relative lack of complex THz filter designs is consistent with a general scarcity of devices that operate effectively in the THz spectral range from 100 GHz to 10 THz, resulting in the well-known THz gap [9]. A variety of different approaches for creating filters in the THz region have been shown. While the majority address band pass filtering, there have also been demonstrations of band stop, high pass, and comb filters [10-18]. Despite these advances, an approach is still needed that allows for versatility in designing a broad range of frequency responses within a single methodology. Plasmonic filters, which are geometrically scalable over a wide range of the electromagnetic spectrum, provide a possible pathway for developing such a methodology to create filters with tailored frequency responses.

4.2 K-Space Design Flow

The primary difficulty in implementing a k-space design process is associated with the issue of fabricating a plasmonic structure that matches the spatial description obtained from the inverse transformed spatial frequency spectrum. Traditional hole arrays allow for only a binary physical representation with a hole present or not; to create a grey-scale physical representation, a different fabrication technique is required. We employ an ink-jet printing technique that allows for the deposition of varying levels of a conductive silver ink or the simultaneous deposition of conductive silver ink and resistive

carbon ink [7]. In this latter printing mode, the conductivity can be spatially controlled, which corresponds to grey scale plasmonic response (i.e., the propagation length of surface plasmon-polaritons (SPPs) can be varied by changing the local conductivity). Details of the printing process and resulting effect on SPP propagation can be found in the supplemental information and in previous work [7]. To illustrate the possibilities, in Fig. 4.1a, we show an artistic rendering of a plasmonic THz filter in which both carbon and silver ink are used to create a spatially varying conductivity pattern in which the transmission of THz radiation is higher if polarized along one axis compared to the other. A photo of an actual printed sample exhibiting the desired anisotropic behavior is shown in Fig. 4.1b, along with an accompanying microscope image in Fig. 4.1c. The details of this specific filter are discussed later in this paper.

4.3 THz Comb Filter

We begin by demonstrating the use of this approach in controlling the relative amplitudes of resonances in a comb filter. In Fig. 4.2, we summarize how the amplitudes of two specific resonances can be individually adjusted. In Figs. 4.2a-4.2c, we create two four-fold rotationally symmetric resonances, one at 0.2 THz and a second at 0.4 THz, where the relative amplitudes of the corresponding discrete spots vary in k-space (additional information regarding the real space patterns is given in the supplementary information). Note that the k-space spectrum is restricted to symmetric patterns in order to ensure that the transformed real space image is composed of only real values. The transform from k-space to real space for the different versions of the comb filter show that all three versions have the same underlying structure, but with different contrast

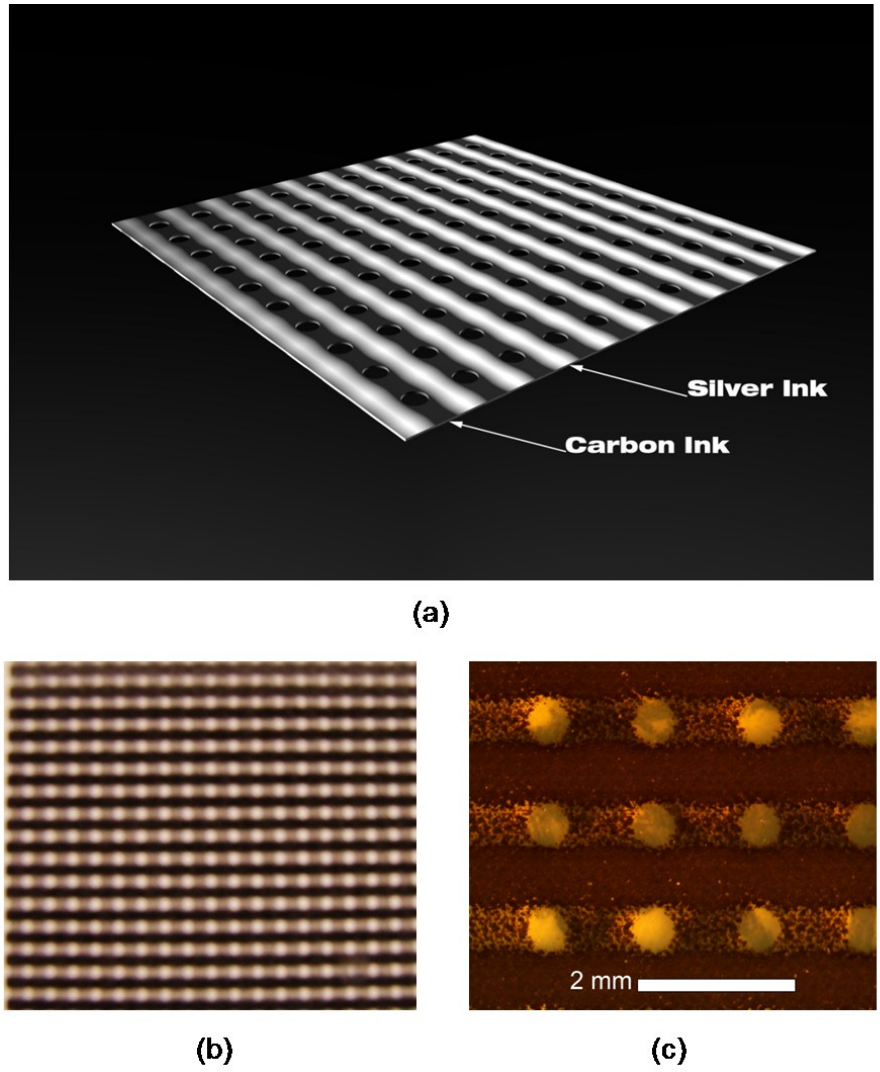

Fig. 4.1. Example of a printed THz filter **a,** Graphical depiction of a physical filter designed in k-space designed to allow for high transmission along one axis and low transmission along the orthogonal axis. This is accomplished by printing a periodic aperture array on a substrate composed of stripes of carbon and silver. The asymmetry in the conductivity along the two axes of the device controls the loss experienced by surface plasmons propagating on the surface of the filter. The detailed operation of the filter is discussed in the paper and summarized in Fig. 4.5. **b,** Photograph of the actual k-space filter depicted in **a**. **c,** The same filter as shown in **a** and **b** but under higher magnification.

between the peaks and valleys of the sinusoidally varying structures. By applying a thresholding algorithm, the different physical space comb images can be viewed as an aperture array designed for 0.2 THz with additional intermediate holes (corresponding to 0.4 THz) darkened according to the weight defined in k-space.

The corresponding real space pattern supports not only these two resonances, but also resonances at 0.24 THz ([2,0] metal-substrate resonance), 0.28 THz ([1,1] metal-air resonance), 0.29 THz ([2,1] metal-substrate resonance), and 0.35 THz ([2,2] metal-substrate resonance), as shown in the measured spectral response in Fig. 4.2d. Several of these additional peaks are due to the asymmetry of the material structure stack. In general, this can complicate k-space filter design by adding additional resonances that can merge together as they are shifted down in frequency. Nevertheless, these substrate contributions may be beneficial in creating more complex comb filters, as is the case in Fig 4.2d, where the comb of frequencies is extended from two resonant peaks to essentially four resonant peaks. Alternatively, the additional resonances can be minimized by overcoating the structure with a medium that is index matched with the 150 μm thick plastic substrate [23]. In Fig. 4.2e, we show the relationship between the designed k-space ratio of the amplitudes of the air [1,0] and [2,0] resonances to the measured ratio of their magnitudes. We find a linear relationship between the designed ratio and the measured ratio. This approach can be extended to incorporate larger numbers of resonances and may be useful in applications where the relative transmittance of several different frequencies needs to be carefully controlled.

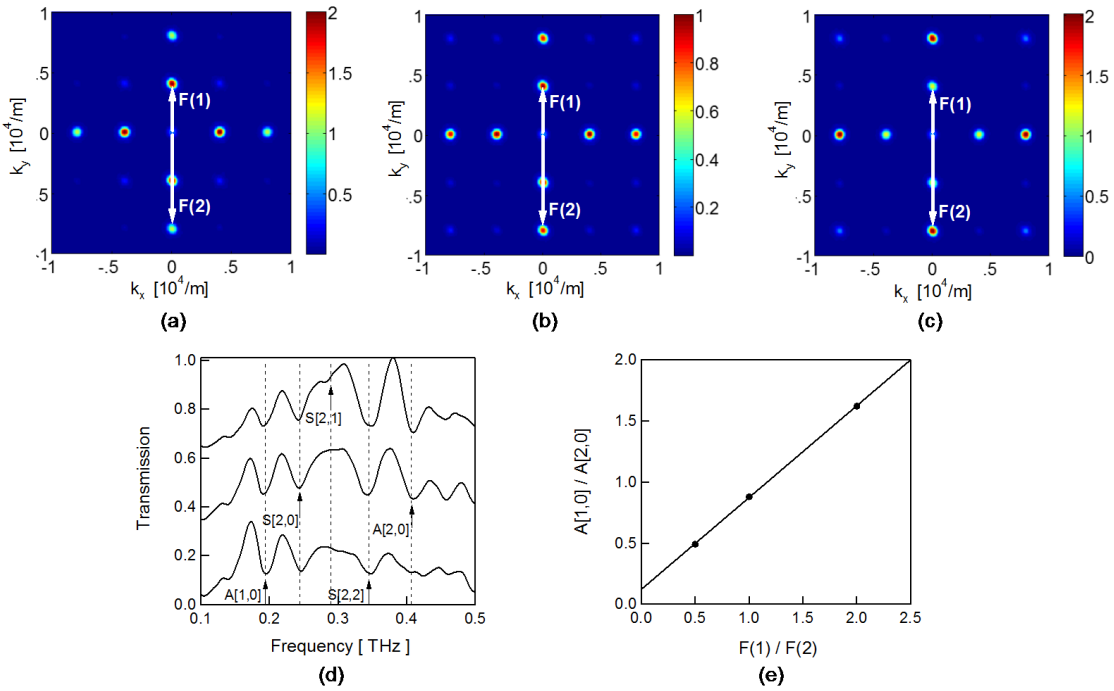

Fig. 4.2. k-space approach for creating THz comb filters with controlled relative amplitudes **a,** k-space representation of a low frequency weighted comb-pass filter. **b,** k-space representation of an equally weighted comb-pass **c,** k-space representation of a high frequency weighted comb-pass filter. **d,** Measured THz spectra for the three filters, where each successive spectrum is offset by a value of 0.3. Along with the two designed resonant peaks at 0.2 THz and 0.4 THz, the spectra also contain features at 0.25 THz, 0.3 THz, and 0.35 THz. These additional peaks are due to the asymmetric material stack. The effect of the plastic sheet can be seen to red shift the [2,0] [2,1] and [2,2] modes of the 0.2 THz holes and the [1,1] mode of the 0.4 THz holes to create the more complicated spectra **e,** Comparison between the ratio of the designed resonant magnitudes and the ratio of the measured resonant magnitudes.

4.4 THz Polarization Sensitive Filter

The k-space approach also allows for the design of polarization dependent filters, where different polarizations of incoming radiation are filtered differently. In Fig. 4.3, we show two different implementations of this idea. In both cases, we design the k-space pattern such that the Reciprocal Vector (RV) corresponds to 0.2 THz along the y-axis and to 0.4 THz along the x-axis. In the first implementation, shown in Fig. 4.3a, this is accomplished using four discrete spots in k-space. The corresponding real space design is shown in Fig. 4.3b. The asymmetry in the locations of the discrete spots creates a stretching effect in the real space aperture geometry. In Fig. 4.3c, we show the measured THz transmittance for each of the two resonance peaks as a function of the incident polarization angle. Both sets of data are fit to an expected sinusoidal variation associated with the projection of incoming radiation onto the k_y and k_x axis, though the variation is somewhat weaker with the higher frequency resonance. The offset from zero transmittance is associated with that fact that some THz radiation is directly transmitted through the holes, while the asymmetry in the response arises from the fact that the "holes" are a different fractional size for the two different resonance frequencies.

The asymmetry in the response can be reduced by drawing a complete ellipse in k-space, as shown in Fig. 4.3d. The resulting real space geometry, shown in Fig. 4.3e, has the appearance of an asymmetric bullseye structure, stretched along the y-axis, although in this pattern, there are low conductivity arcs across the pattern that allow for THz transmission not only through the central aperture, but also through these arcs. The resulting resonance peaks occur at 0.33 THz and 0.16 THz, as shown in Fig. 4.3f. Once again, the magnitude of each resonance peak is characterized by a sinusoidal polarization

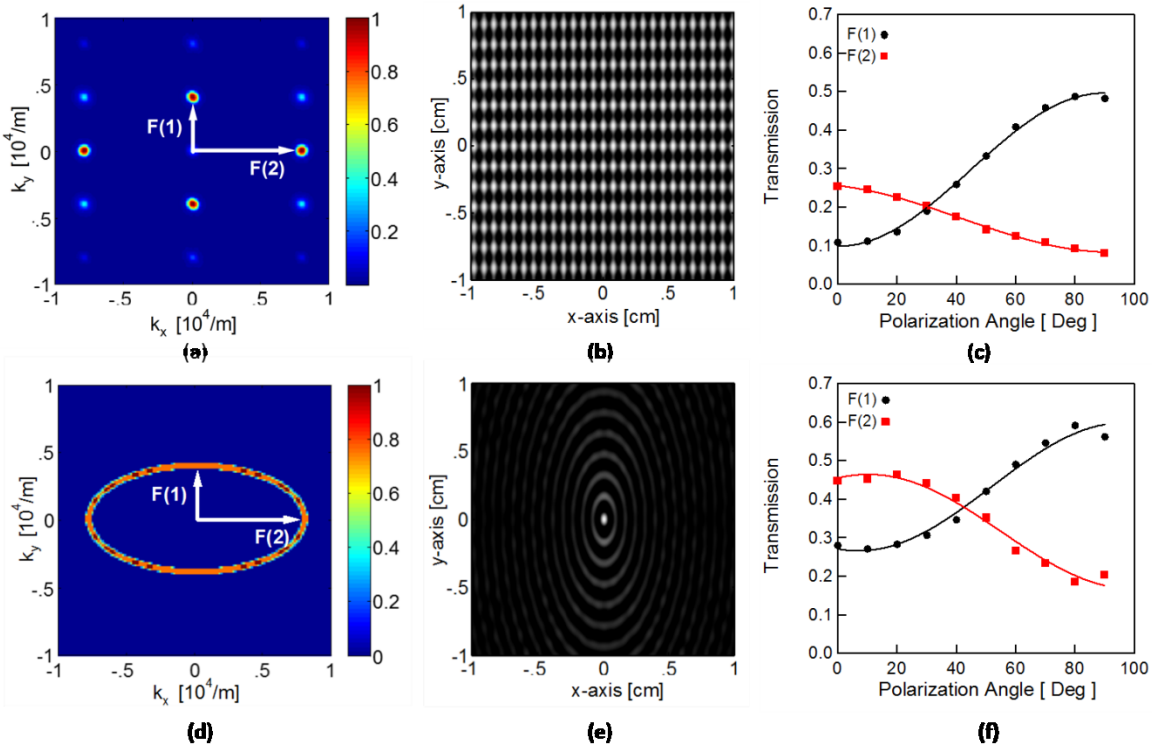

Fig. 4.3. k-space approach for creating polarization sensitive THz filters **a,** k-space representation of a 4 point elliptical filter with resonant peaks placed at higher spatial frequency in k_x than in k_y. **b,** Corresponding 2D spatial image obtained from the inverse Fourier transform. The stretching effect on the holes due to the asymmetry can be clearly seen. **c,** Measured transmission as a function of the polarization angle at two distinct resonant peaks located at 0.15 THz and 0.34 THz. **d,** k-space representation of a full ellipse with resonant peaks varying from a higher spatial frequency in k_x to a lower spatial frequency in k_y. **e,** Corresponding 2D spatial image obtained from the inverse Fourier transform. **f,** Measured transmission as a function of the polarization angle at 0.16 THz and 0.33 THz.

dependence. It is worth noting that the measured spectra of previous bullseye structures [24] are fully consistent with the predicted k-space design approach described here.

4.5 THz Highly Anisotropic Filter

We can also demonstrate an anisotropic filter similar to the filters described in Fig. 4.3. However, instead of shifting the frequencies of the resonant peak or the relative magnitudes of multiple peaks, here we control the magnitude of the sinusoidal variation associated with the transmission peak of a single resonance by changing the polarization of the incoming light. In Fig. 4.4a, we show a 2-fold symmetric filter that, in k-space, has a magnitude at 0.2 THz that is four times as large along k_y as it is along k_x. This results in a real space geometry, shown in Fig. 4.4b, where the image contrast along one axis of the image is four times greater than that along the orthogonal axis. In Fig. 4.4c, we show the magnitude of the transmission resonance peak at 0.18 THz as a function of the incident polarization. Since this approach operates only on a single resonance, the amplitude ratio (maximum/minimum transmission = 5) is larger than that observed in Fig. 4.2. The magnitude of this anisotropy can also be varied. In Fig. 4.4d, we show the contrast (ratio of the maximum to the minimum amplitude) for anisotropy values ranging from 1.25:1 to 4:1. This contrast ratio is found to vary linearly with the magnitude of the k-space anisotropy.

4.6 THz Band Pass Filter

This breadth of potential designs for complex plasmonic filters can be significantly expanded if we now consider the possibility of cascading sequential linear

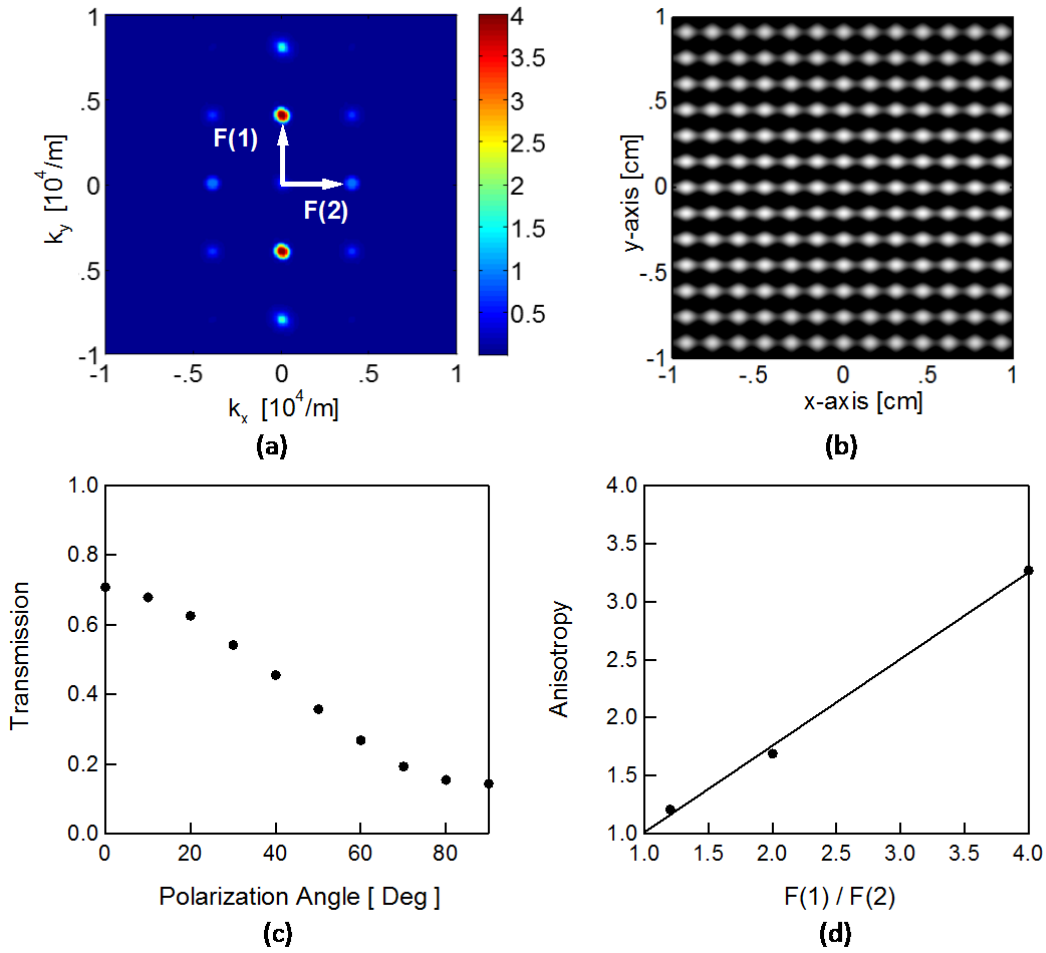

Fig. 4.4. k-space approach for creating THz filters with controlled polarization sensitivity for a single resonance. **a,** k-space representation of the anisotropic filter with a larger magnitude resonant peak along k_y than to k_x. **b,** Corresponding 2D spatial image obtained from the inverse Fourier transform **c,** Transmission as a function of the polarization angle. **d,** Enhancement factor as a function of the ratio of the magnitude of the resonances along k_y and k_x. The enhancement factor corresponds to the ratio of the maximum to minimum transmission. The line represents a least-squares linear fit to the data.

filters into a single filter. Such an operation typically requires performing a convolution of two or more filter functions, typically in the real space domain, or a multiplication of the corresponding filter functions in the conjugate k-space domain. In general, the convolution can take place in either the real space or k-space domain to create more complex filter functions. Alternatively, complex filter functions can be obtained by simply adding filter functions, yielding a response that may not be straightforward to achieve by other means. We give two examples to demonstrate the utility of this general approach.

In the first example, we demonstrate the ability to control the bandwidth of a bandpass filter. In Fig. 4.5a, we show the k-space representation of an 8-fold symmetric bandpass filter, along with its inverse transformed real space geometry in Fig. 4.5b. To control the bandwidth of the filter, a Gaussian soft aperture was used to weight the k-space image (by convolving filter functions in k-space or performing multiplication in real space), yielding a real space pattern that included an additional Gaussian spatial modulation (i.e., took on grey scale values). An example of such a structure obtained using a soft aperture with a bandwidth of 33 GHz is shown in Fig. 4.5c.

In Fig. 4.5d, we show the measured spectral response for a filter without a soft aperture. The lowest order resonance, corresponding to the F(1) reciprocal vector (RV), corresponds to 0.3 THz for the metal-air interface and 0.195 THz for the metal-substrate interface [20]. The lower frequency resonance arises from the fact that the plastic substrate has a measured THz refractive index of $n_{THz} = 1.54$ across the THz spectral range of interest. Note that the frequencies associated with the RVs correspond to the

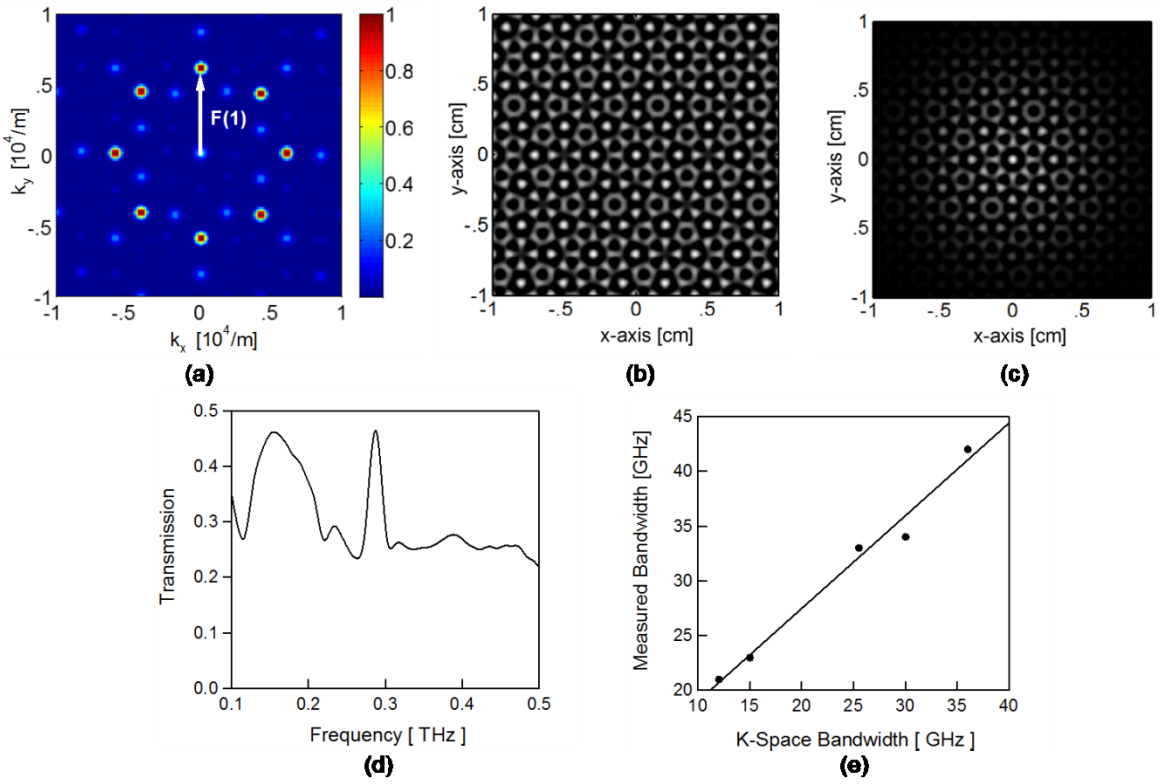

Fig. 4.5. k-space approach for creating THz filters with controlled bandwidth **a,** k-space representation of a 0.3 THz 8-fold symmetric narrow band-pass filter. **b,** 2D-spatial image obtained from an inverse Fourier transform of the k-space representation in **a**. **c,** Spatial representation of a conductivity weighted soft Gaussian aperture applied to the image in **b**, which allows for control over the bandwidth of the filter **d,** Measured THz spectrum for the printed device. **e,** Measured bandwidth of 6 filter samples as a function of the designed k-space bandwidth. The line represents a linear least-squares fit to the data.

amplitude dips on the high frequency sides of the resonances and that the resonance peaks occur at a somewhat lower frequencies [21]. In Fig. 4.5e, we show the measured amplitude dips on the high frequency sides of the resonances and that the resonance peaks occur at a somewhat lower frequencies [21]. In Fig. 4.5e, we show the measured bandwidth of the metal-air resonance for 5 different soft aperture widths, where a wider opening corresponds to a narrower bandwidth. The linear fit to the data shows good agreement between the designed k-space bandwidth and the measured bandwidth. The lack of exact numerical agreement between the two arises from the fact that real metals exhibit loss, which is not incorporated in the design technique. It may be noted in Fig. 4.5d that the roll off and stop band extinction of the filter are not particularly high. This is because the frequency response is only a first order response. Because these plasmonic filters operate in the linear regime, a multilayer stack of such filters can create an overall frequency response that is given simply by the product of the transmittance of each individual filter. Though it is beyond the scope of the present work, this approach has been shown to greatly increase the roll off and stop band extinction [22].

4.7 THz Geometrical Controlled Filter

In the second example, we demonstrate a filter response that arises from the superposition of two distinct k-space objects. In Fig. 4.6a, we show the k-space spectrum of two superposed geometric shapes, a rectangle and a variably weighted circle. Because these two shapes have different symmetry properties, they will have different polarization dependent contributions to the overall frequency response of the filter. The rectangular shape corresponds to a resonance at 200 GHz along the k_y direction and a resonance at

400 GHz along the k_x direction, while the weighted annulus corresponds to a polarization independent resonance frequency of 400 GHz.

Fig. 4.6b shows the real space image obtained from an inverse Fourier transform of the k-space rectangle, with the weighting value of the annulus, W, set to zero (effectively leaving only the rectangle). As the weighting value of the annulus, W, is increased, its effect on the real space structure can be seen in Fig. 4.6c and 4.6d. With increasing values of W, the real space structure becomes increasingly rotationally symmetric. When W is set to zero and the filter exhibits only the anisotropic contribution from the rectangle in k-space, the measured ratio of the transmission magnitude at the two resonant frequencies, |F(2)/F(1)|, will vary with the polarization angle as shown in Fig. 4.6e. As the weight of the annulus is increased, the ratio |F(2)/F(1)| is also increased, while maintaining same polarization dependency, creating the ability to control the relative magnitudes of different resonances. More generally, the ability to combine multiple filter functions, where each function may be weighted differently, offers the opportunity to create a range of unique THz filter capabilities.

In summary, we have proposed a novel THz filter design methodology that involves defining the k-space representation of a desired filter and then transforming it to obtain the real space geometry for the device. Using conventional ink-jet printers, we external stimuli or the incorporation of other materials that are active should allow for the fabrication of dynamic filters. Further exploration of this approach is expected to lead to new optoelectronic device capabilities that may be useful for THz applications, which is largely devoid of device and systems technology.

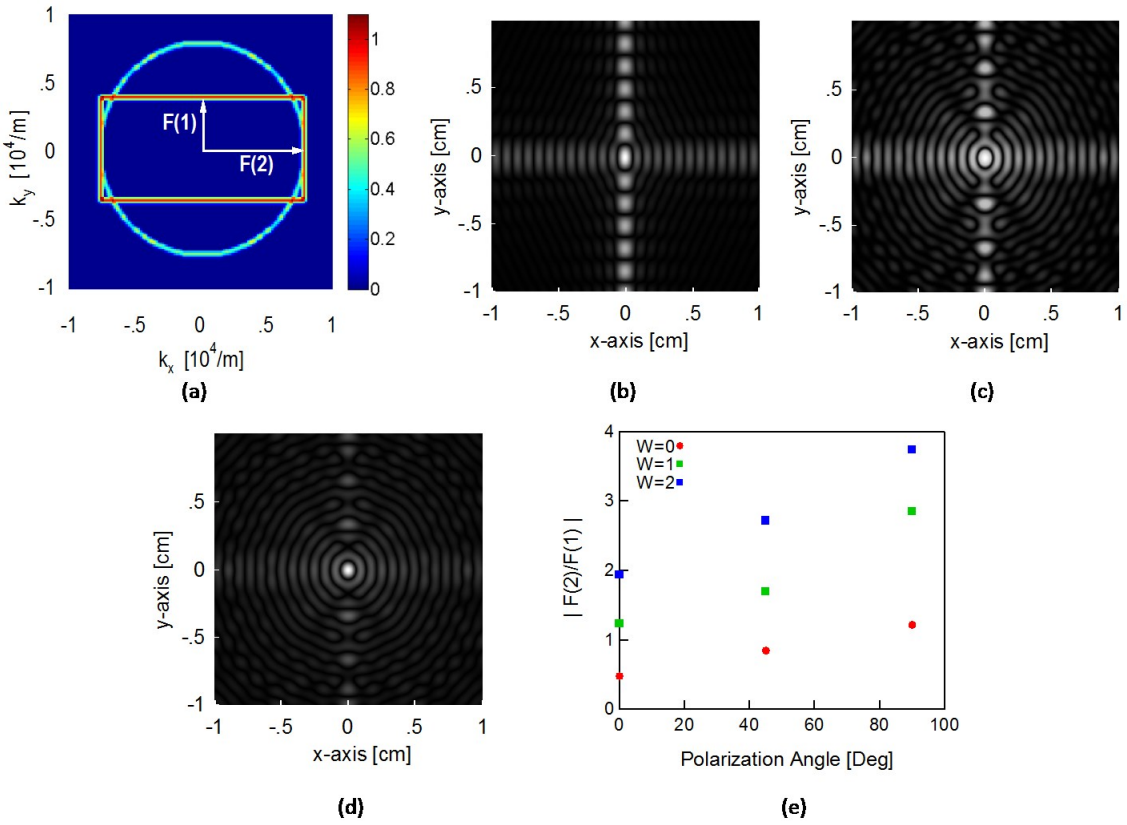

Fig. 4.6. k-space approach for creating THz filters with controlled geometric anisotropy. **a,** k-space representation of the rectangular anisotropic filter with resonant frequencies of 200 GHz and 400 GHz along k_y and k_x, respectively (with a weighting factor of 1), superimposed with a circularly symmetric annulus weighted by a factor W, with resonant frequency at 400 GHz. **b,** Corresponding 2D spatial image obtained from the inverse Fourier transform of **a**, with the 400 GHz ring weighted at 0 **c,** Corresponding 2D spatial image obtained from the inverse Fourier transform of **a**, with the 400 GHz ring weighted at 1. **d,** Corresponding 2D spatial image obtained from the inverse Fourier transform of **a**, with the 400 GHz ring weighted at 2. **e,** Measured ratio of the transmission, |F(2) / F(1)| as a function of the polarization angle.

4.8 References

1. Akagi, H. New trends in active filters for power conditioning. *Industry Applications, IEEE Transactions on* **32,** 1312–1322 (1996).

2. Rader, C. M. & Gold, B. Digital filter design techniques in the frequency domain. *Proc. IEEE* **55,** 149–171 (1967).

3. Frerking, M. E. *Digital signal processing in communication systems*. (Van Nostrand Reinhold, 1994).

4. Glance, B., Kaminow, I. P. & Wilson, R. W. Applications of the integrated waveguide grating router. *J. Light. Technol.* **12,** 957–962 (1994).

5. Pozar, D. M. *Microwave engineering*. (Wiley, 2009).

6. Madsen, C. K. & Zhao, J. H. *Optical filter design and analysis*. (John Wiley, 1999).

7. Gupta, B., Pandey, S., Guruswamy, S. & Nahata, A. Terahertz plasmonic structures based on spatially varying conductivities. *Adv. Opt. Mat.* 1–7 (2014). doi:10.1002/adom.201400018.

8. Koenig, S. *et al.* Wireless sub-THz communication system with high data rate. *Nat. Photon.* **7,** 977–981 (2013).

9. Tonouchi, M. Cutting-edge terahertz technology. *Nat. Photon.* **1,** 97–105 (2007).

10. Porterfield, D. W. *et al.* Resonant metal-mesh bandpass filters for the far infrared. *Appl. Opt.* **33,** 6046–6052 (1994).

11. Gupta, S., Tuttle, G., Sigalas, M. & Ho, K.-M. Infrared filters using metallic photonic band gap structures on flexible substrates. *Appl. Phys. Lett.* **71,** 2412–2414 (1997).

12. Winnewisser, C., Lewen, F. T., Schall, M., Walther, M. & Helm, H. Characterization and application of dichroic filters in the 0.1-3-THz region. *Microwave Theory and Techniques, IEEE Trans.* **48,** 744–749 (2000).

13. MacDonald, M. E., Alexanian, A., York, R. A., Popovic, Z. & Grossman, E. N. Spectral transmittance of lossy printed resonant-grid terahertz bandpass filters. *Microwave Theory Techniques, IEEE Trans.* **48,** 712–718 (2000).

14. Wu, D. *et al.* Terahertz plasmonic high pass filter. *Appl. Phys. Lett.* **83,** 201–203 (2003).

15. Drysdale, T. D. *et al.* Transmittance of a tunable filter at terahertz frequencies. *Appl. Phys. Lett.* **85,** 5173–5175 (2004).

16. Cunningham, J. *et al.* Terahertz frequency range band-stop filters. *Appl. Phys. Lett.* **86,** 213503–213503 (2005).

17. Paul, O., Beigang, R. & Rahm, M. Highly selective terahertz bandpass filters based on trapped mode excitation. *Opt. Express* **17,** 18590–18595 (2009).

18. Mendis, R., Nag, A., Chen, F. & Mittleman, D. M. A tunable universal terahertz filter using artificial dielectrics based on parallel-plate waveguides. *Appl. Phys. Lett.* **97,** 131106–131106 (2010).

19. Grischkowsky, D., Keiding, S., Van Exter, M. & Fattinger, C. Far-infrared time-domain spectroscopy with terahertz beams of dielectrics and semiconductors. *J. Opt. Soc. Am. B* **7,** 2006–2015 (1990).

20. Ebbesen, T. W., Lezec, H. J., Ghaemi, H. F., Thio, T. & Wolff, P. A. Extraordinary optical transmission through sub-wavelength hole arrays. *Nature* **391,** 667–669 (1998).

21. Matsui, T., Agrawal, A., Nahata, A. & Vardeny, Z. V. Transmission resonances through aperiodic arrays of subwavelength apertures. *Nature* **446,** 517–521 (2007).

22. Nguyen, T. D., Liu, S., Vardeny, Z. V. & Nahata, A. Engineering the properties of terahertz filters using multilayer aperture arrays. *Opt. Express* **19,** 18678–18686 (2011).

23. Krishnan, A. *et al.* Evanescently coupled resonance in surface plasmon enhanced transmission. *Opt. Comm.* **200,** 1–7 (2001).

24. Cao, H., Agrawal, A. & Nahata, A. Controlling the transmission resonance lineshape of a single subwavelength aperture. *Opt. Express* **13,** 763–769 (2005).

CHAPTER 5

CONCLUSION

In summary, we have proposed a novel THz filter design methodology by initially defining the k-space representation of a desired filter which is then used to determine the physical parameters for the device. By taking the inverse 2D-Fourier transform of the k-space representation a 2D-spatial image is obtained that is used in fabricating the desired filter. In addition to using k-space design tools controlling the hole radius in plasmonic filters enables additional control over the transmittance of designed filters. The results in this thesis suggest statistically weighting the hole sizes in a quasi-periodic plasmonic structure is a viable way to tune the frequency response of a filter. Variation of the relative magnitudes of the two resonances in the filter is significant as it allows for a new degree of control in filter design.

This kind of filtering capability would be required in a THz Frequency Shift Keyed (FSK) communication system where two distinct carrier frequencies are used to transmit information through a wireless channel. Due to frequency selective fading in a physical channel, the carrier frequencies power needs to be equalized at the receiver after propagating through the channel. This works demonstrates a THz filter design methodology that allows variable power transmission control over the individual

frequency components of the filter. This new capability helps fill in one of the gaps in a realizable THz FSK system. This filtering approach might also be useful in more fundamental research in allowing one to flatten the output spectrum of a THz emitter.

We have demonstrated several more complex k-space designed filters using an off the shelf ink-jet printer with conductive silver ink to directly fabricate the 2D-spatial image obtained from k-space. Using this technique we demonstrated: two band-pass filters with identical center frequencies at 250GHz but different bandwidths, comb-pass filters where the relative magnitudes of individual resonant peaks at 200, 245, 345 and 400GHz are shifted by approximately 50 percent from low frequencies to higher frequencies in the comb, a polarization dependent filter that shifts the magnitude between two resonant peaks at 150 and 345GHz up and down by 70 percent based on a polarization angle change from 0 to $\pi/2$, and finally a filter with a transmittance that varies by 80 percent at a single resonant frequency based upon the polarization angle of incoming radiation from 0 to $\pi/2$. Using this k-space approach to THz filter design enables more complex filters that could find application in THz modulators and wireless communication systems.